STARS

Electronic Theses and Dissertations, 2020-

2022

Light Trapping Transparent Electrodes

Mengdi Sun
University of Central Florida

University of
Central
Florida

STARS
Showcase of Text, Archives, Research & Scholarship

LIGHT-TRAPPING TRANSPARENT ELECTRODES

by

MENGDI SUN
B.S. Huazhong University of Science and Technology, 2015
M.S. University of Florida, 2017

A dissertation submitted in partial fulfillment of the requirements
for the degree of Doctor of Philosophy
in College of Optics and Photonics, CREOL,
at the University of Central Florida
Orlando, Florida

Spring Term
2022

Major Professor: Pieter G. Kik

ABSTRACT

Transparent electrodes represent a critical component in a wide range of optoelectronic devices such as high-speed photodetectors and solar cells. Fundamentally, the presence of any conductive structures in the optical path leads to dissipation and reflection, which adversely affects device performance. Many different approaches have been attempted to minimize such shadowing losses, including the use of transparent conductive oxides (TCOs), metallic nanowire mesh grids, graphene-based contacts, and high-aspect ratio metallic wire arrays.

In this dissertation I discuss a conceptually different approach to achieve transparent electrodes, which involves recapturing photons initially reflected by highly conductive electrode lines. To achieve this, light-redirecting metallic wires are embedded in a thin dielectric layer. Incident light is intentionally reflected toward large internal angles, which enables trapping of reflected photons through total internal reflection (TIR). Light trapping transparent electrodes could potentially reach the holy grail of transparent electrodes: the simultaneous achievement of high conductivity and near-complete optical transparency. We numerically and experimentally investigate several light trapping electrode structures. First, we study the spectral and angular optical transmission of embedded interdigitated metallic electrodes with inclined wire surfaces and demonstrate efficient broadband angle-insensitive polarization-independent light trapping. Proof-of-principle experiments are carried out, demonstrating several of the features observed in our numerical studies. Second, a novel type of grating-based light trapping transparent electrode is discussed. In this approach, diffraction from metal wires covered with nanoscale silicon gratings is used to achieve total internal reflection. We show that careful grating optimization achieves

strong suppression of specular reflection, enabling a more than fivefold reduction of shadowing losses. The realization of a high light-trapping efficiency in a coplanar structure makes the design a promising candidate for integration in real-world optoelectronic devices. Finally, the transmission of high-index metasurfaces is investigated. Such structures may enable efficient light redirection around metallic contacts, if reflection losses by the metasurface can be suppressed. We demonstrate that the traditional anti-reflection coating approach fails for such structures, and present an improved design approach that reduces reflection losses over a broad range of structural parameters.

To my family, friends and those who have helped me in my life.

ACKNOWLEDGEMENTS

It has been a long time since I first visited CREOL in 2017. I still remember how excited I was when I got admitted and decided to pursue a doctorate degree here. During the 5-year journey towards my PhD, I was so fortunate to have received help and support from many people. Now at the end of this long journey, I wish to express my sincere appreciation to all of them.

First and foremost, I would like to express my utmost gratitude to my advisor Dr. Pieter G. Kik, who has always been supportive and willing to help for the past five years. It is a pleasure to work with him for his patience, wisdom, enlightening suggestions and consistent encouragement, especially during the hard time of the global pandemic. He always holds high standards in research, including scientific thinking, physical interpretation, academic writing and presentation skills, which will benefit me for my entire life.

Besides, I would like to acknowledge my thesis advisory committee, Dr. Stephen M. Kuebler, Dr. Kristopher O. Davis and Dr. C. Kyle Renshaw for their insightful comments and kind support in my research. I really enjoy the collaborations with their groups and did learn a lot from them.

I would like to thank my colleagues and friends in CREOL. Dr. Mohammod Jobayer Hossain collaborated with me on two excellent papers on photovoltaic solar cells, from which I obtained great knowledge on photovoltaics and semiconductor devices. Pooria Golvari and Di Huang helped me a lot on device fabrication and measurements so that I could rapidly push forward my research project. Dr. Oussama Mhibik, Dmitrii Konnov, He Cheng, Laurence Trask, Dr. Xiaoming Yu Dr. Peter J. Delfyett and Dr. M. G. Jim Moharam offered great help to me when I

TABLE OF CONTENTS

LIST OF FIGURES

CHAPTER 1: INTRODUCTION

1.1 Background

Transparent electrodes (TEs) are widely used in optoelectronic devices such as solar cells, photodiodes, photovoltaic devices, displays and transparent heaters [1-4]. These devices suffer from shadowing losses caused by the reflection and absorption of incident light by the electrodes [5]. In photovoltaic (PV) cells, electrical contacts are necessary to collect charge carriers, which is commonly achieved using metallic wires [6]. However, the metallic nature of the contacts inevitably causes shadowing loss, dominated by reflection losses. In order to minimize the shadowing loss and maintain high electrical conductivity at the same time, a sparse array of thin metallic wires is commonly used. In organic light emitting diodes (OLEDs) electrical contacts are needed to inject charges, while one side of the device needs to be transparent to allow light emission. In these devices thin conducting films such as indium-tin-oxide (ITO) are typically used. Another application of transparent electrodes involves transparent film heaters (TFHs) [7]. TFHs rely on resistive heating to avoid condensation and frosting, and are used for example in vehicles, in outdoor panel displays, and specialized cameras [8-10].

In most devices that use transparent electrodes, there is an intrinsic trade-off between transparency and conductivity. In the case of conductive wire electrodes, a minimum areal coverage of metal is needed for achieving low sheet resistance. In the case of thin-film conductive layers, a minimum thickness is required for achieving small sheet resistance, which is accompanied by absorptive loss related to dissipation by the charge carriers. Consequently, for both approaches

there is an intrinsic trade-off between transparency and conductivity. The large difference in conductivity between metals and typical transparent oxides (Figure 1.1) leads to different design decisions [11]. A third possible approach for achieving transparent electrodes that largely avoids this trade-off involves routing light around the conductive regions, typically done using refractive structures, e.g. lens arrays [12].
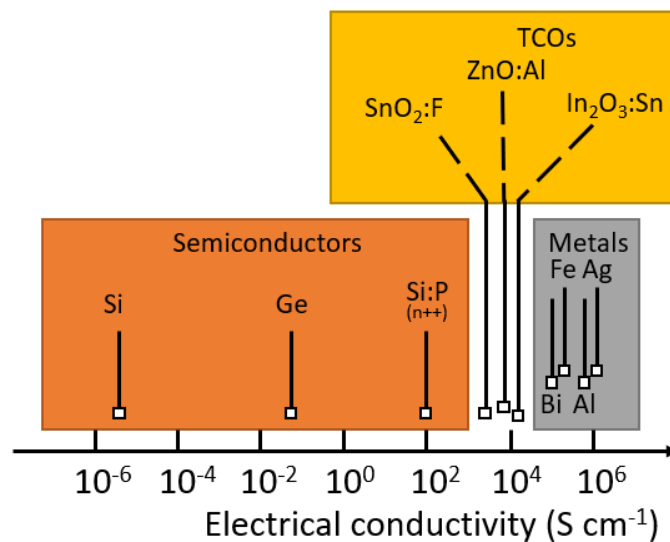
Figure 1.1: Electrical conductivities of different materials.

1.2 Current progress of transparent electrodes

Conventional transparent electrodes can broadly be divided into three categories: thin film electrodes, random mesh grids, and wire arrays, each with their own specific challenges in achieving high conductivity and high transparency. Various transparent conductive materials (TCMs) are used in TEs. In general, high optical transparency and electrical conductivity are

needed for optoelectronic devices. Additionally, mechanical stability, cost, and simplicity of fabrication are desirable. Different TEs and their fabrication processes are reviewed in this chapter.

Transparent conductive oxides (TCOs) are widely used as the electrical anode due to their relatively high conductivity and good optical transparency. The electrical conductivity of these materials can be controlled by changing the material composition and thermal treatment. Various TCOs have been employed as TEs, such as indium tin oxide (ITO), zinc oxide and titanium oxide. Among these, ITO is the most commonly used. ITO has relatively high electrical conductivity and optical transparency. For a 100 nm thick ITO layer on glass substrate, a sheet resistance of 10 Ω/sq with more than 90% transmittance can be achieved [13]. ITO has excellent broadband optical transmittance in visible and infrared [14]. However, several disadvantages of ITO limit its overall performance. Firstly, the scarcity of indium results in the high price of ITO, which prevents it from mass production [15]. Secondly, when deposited on the semiconductor or organic semiconductor substrate, the migration of indium into the substrate is the main reason of device degradation [16]. Apart from this, low mechanical stability, including mechanical flexibility and high brittleness, represents a challenge [17]. Moreover, the low work function (4.7 eV) limits the efficiency of hole injection, which is a critical issue in OLED displays [18].

Graphene is an emerging nanomaterial with exceptional material properties. Graphene consists of a 2D hexagonal lattice of carbon atoms [19]. Graphene is a monolayer material and the thickness of a single graphene layer is thus atom-scale [20]. Graphene has a high carrier mobility, so it has excellent electrical conductivity given its thickness. However, increasing the sheet conductivity by using multilayer graphene faces challenges. High quality graphene is also difficult to fabricate.

Conductive polymers are a group of organic polymers that conduct electricity. The most commonly used conductive polymer as transparent conductive material is Poly(3,4-ethylenedioxythiophene) (PEDOT:PSS), which is a Sulfur-containing conductive polymer [21]. Conductive polymers are widely used in optoelectronic devices such as organic light emitting diodes (OLEDs) and organic photovoltaics (OPVs) [22]. Conductive polymers have combined optical and electrical properties: it was demonstrated that thin PEDOT:PSS films (less than 100 nm) has a sheet resistance of 240 Ω/sq and 97% optical transmittance under 550 nm illumination [23]. However, conductive polymers have relatively large sheet resistance compared to ITO. Consequently, conductive polymers cannot replace ITO in devices that require high conductivity. Moreover, low long-term chemical stability is another concern for conductive polymers [24].

Thin film metallic TEs would be highly reflective unless the thickness is almost negligible. To address this issue, the incident light needs to avoid the electrodes to reduce the shadowing loss. Therefore, it is necessary for highly conductive regions to only cover a small fraction of the surface areas while leaving the most areas open. This is the basis of wire-based electrodes. In general, wire-based electrodes can be divided into two categories: random mesh grids and wire arrays. Here we review the properties and fabrication process of random mesh grids first.

Carbon nanotubes (CNTs) are nanomaterials that contain a two-dimensional hexagonal lattice of carbon atoms arranged to form an atomically thin cylinder [25]. CNT mesh electrodes are used in organic and inorganic photovoltaic solar cells [26]. CNTs have been shown to enable good combined optical and electrical performance. It was demonstrated that CNTs could achieve a sheet resistance of 60 Ω/sq and 90.9% optical transmittance simultaneously [27]. Owing to the

covalent bonds between adjacent carbon atoms, CNT has outstanding mechanical strength and stiffness [28].

Nevertheless, the optoelectronic performance of CNT based transparent electrodes is not comparable to that of ITO. Owing to high junction resistance at the connection between different CNTs, carbon nanotube networks have relatively high sheet resistance [29]. In addition, the existence of semiconductor type CNTs inside the mesh will increase absorption and lead to reduced optical transparency [30].

Metallic nanowire (MNW) based transparent electrodes exhibit good optical and electrical properties. Metallic nanowire based TEs include copper, silver, gold and nickel alloy nanowires [31]. Metals have a large free charge density, leading to extremely large conductivity. For metals commonly used as TEs such as copper, silver and gold, the plasma frequency occurs in the visible or near-UV region of the spectrum, and consequently strong reflection is anticipated.

Interestingly the conductivity of metal nanowires is not only determined by the wire cross-section. When the diameter of the nanowires approaches the mean free path of electrons in bulk metals, the electrical conductivity decreases drastically [32]. This is due to the scattering of electrons on the surface of the wires, which results in extra resistivity. On the other hand, reduced wire diameters will reduce optical scattering losses. The electrical conductivity of MNWs is also affected by the contact resistance between different wires in the mesh. This can be reduced by post-deposition thermal annealing, chemical treatments, laser sintering, light-induced plasmonic nano-welding and mechanical pressing [33-35]. Such methods can significantly reduce the sheet resistance from 10^7 to 9.5 Ω/sq [36]. Accordingly, MNWs show higher electrical conductivity over other materials [37].

1.3 Light trapping transparent electrodes

In order to minimize the shadowing losses in metal wire array electrodes, a small metal fill fraction is needed. However, the reduced cross-sectional area of the electrode and the large open area will lead to low sheet conductivity. To achieve high conductivity and low shadowing losses, different approaches are used to minimize light interaction with any metallic surfaces, either through light redirection around the wires, or light trapping of reflected light.

The aspect ratio of an electrode is defined as the ratio between its height and width. High aspect ratio electrodes can be used as TEs for their ability to redirect light. Atwater et al. reported a computational study of metallic mesoscale light trapping electrode with high aspect ratio in 2018 [38]. Structures with different sizes were compared. The schematics are shown in Figure 1.2. For triangular electrodes with high aspect ratio, incident light is reflected in a large angle to surface normal and redirected into the substrate. This angle is the complementary angle of the top angle of the cross-sectional triangle. The study showed that small devices (w=50-1000 nm) exhibited strong dissipation, while electrodes in mesoscale sizes (w>1 μm) showed better performance. It was shown that 99% optical transmittance with a sheet resistance of 0.1 Ω/sq can be achieved with 20% areal metal coverage, 5 μm width and 15 μm height. Besides, an absorption enhancement of up to 15% in 2 μm thick silicon substrate covered by dense electrode arrays was observed.
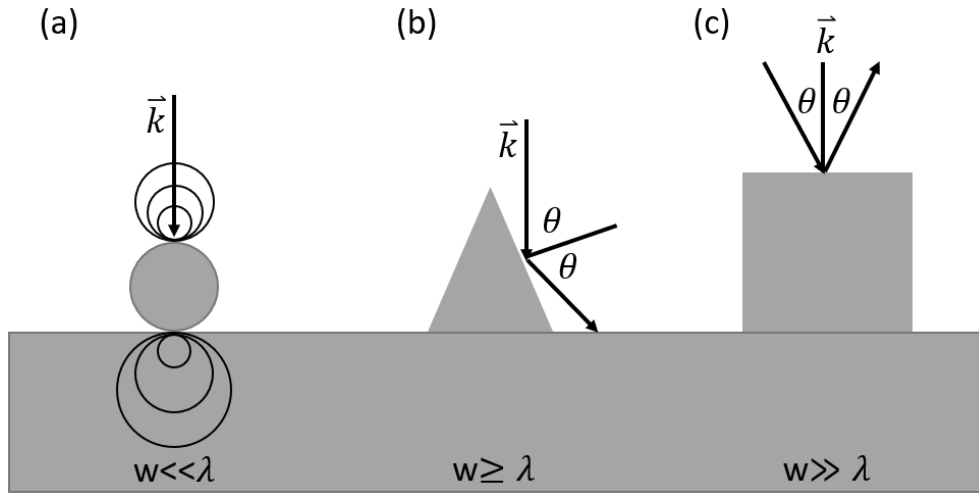
Figure 1.2: Schematics of (a) nanoscale (b) mesoscale and (c) microscale metallic nanowires.

However, high aspect ratio electrodes are difficult to fabricate. Moreover, this kind of structure is mechanically instable and could be more susceptible to cracking than low-aspect ratio wires when being bent or extended. Limited adhesion to the substrate is another challenge in this configuration.

An advanced approach related to the previous section is the use of cloaked contacts. The idea of invisible contacts using metamaterials was presented by Pendry et al in 2006 [39]. Recently Martin *et al.* have developed its applications as transparent electrodes on solar cells [40]. Incident light is redirected to avoid interaction with the object (e.g. wire electrode), while maintaining the propagation angle after leaving the cloak. This is a key difference with the lens array approach discussed above. The refractive index of the material ranges from 1-1.5, which is practical in common materials like polymers or silica glass. This layer is designed to be graded-indexed to redirect the incident light to avoid the contacts and get absorbed.

Other than high-aspect ratio or encapsulation, contacts with engineered reflective properties also enable enhanced optical transparency. A light trapping silver electrode was proposed by Kik in 2014 [41]. In this work a semi-triangular geometry incorporated with a dielectric cover layer was employed to improve the optical performance. The schematic is shown in Figure 1.3. A silver electrode with tilted surface is embedded in a dielectric layer. As shown in Figure 1.3, normally incident light is reflected at high angle, resulting in total internal reflection (TIR) at the surface of the dielectric layer, resulting in back-reflection into the substrate. Based on the ray optics analysis, 100% frequency and polarization independent optical transmission can be achieved for this structure at 50% metal areal coverage, by entirely eliminating reflection losses.
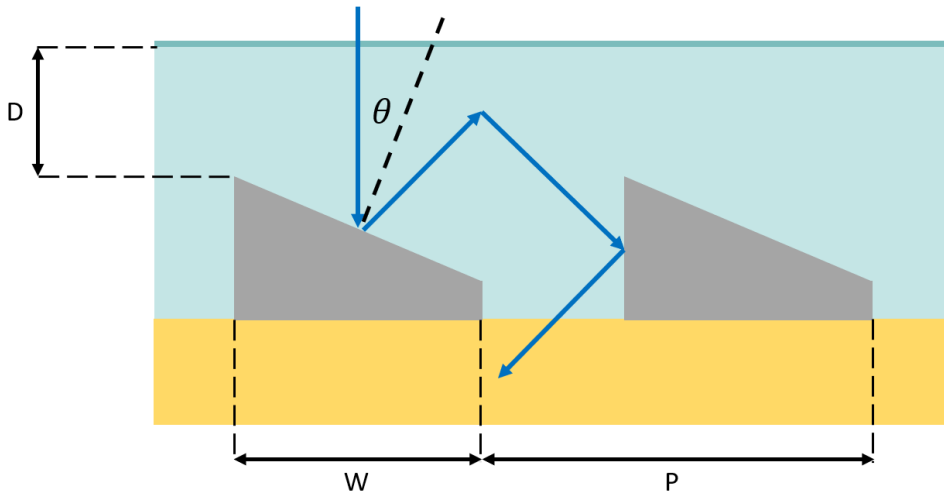
Figure 1.3: The schematic of the semi-triangular Transparent electrodes.

Light-trapping cylindrical nanowire TEs are substantially adopted due to facile fabrication process. Fan et al. reported a numerical analysis of cylindrical silver nanowire electrodes embedded in silicon nitride cover layers [42]. A generalized Fabry-Perot model was developed to study the optical characteristics of the device. As a result, a broadband antireflection performance

in visible and near infrared range was demonstrated for the electrodes. Absorption becomes significant in short wavelength (400-600 nm) for TM polarized waves due to plasmon-assisted absorption. It was also proved that the optical performance of the device is angular independent at small incident angles.

1.4 Metasurfaces and flat optics for shadowing loss reduction

Flat optics is an emerging field of optics that aims at replacing traditional bulky optical elements with subwavelength gradient phase arrays, commonly called gradient metasurfaces. By imparting specific phase profiles on the optical wavefront through specifically tailored non-periodic nanostructures arbitrary wavefront control is achieved, allowing the development of thin (typically few-wavelength) optical components. Due to the rapidly development of computational algorithms and fabrication techniques originated from the semiconductor industry, large-scale design and production of complex metasurfaces has become possible in recent years. Metasurfaces have a variety of applications, including imaging [43], sensing [44-46], beam-steering [47] and holographic displays [48, 49]. Aside from passive devices, active metasurfaces incorporating dynamically tunable materials such as Metal-oxide-semiconductors (MOS) [50] and phase change materials (PCM) [51, 52] have also attracted attention from both academia and industry. Metalenses and beam steering metasurfaces can focus or steer incident light. By placing these metasurfaces on the front side of photodetectors or solar cells, the incident light could be redirected into the substrate while largely avoiding metallic contacts, substantially reducing the shadowing

losses. Therefore, metasurfaces and other flat optics elements could be incorporated in novel transparent electrode designs.

1.5 Summary

This dissertation is organized as follows: Chapter 2 investigates the size-dependent performance of metallic light trapping electrodes with triangular and circular cross-section. Chapter 3 addresses the angle-dependent transmission of triangular transparent electrodes. Chapter 4 presents an experimental demonstration and optical characterization of triangular light trapping electrodes fabricated through multi-photon lithography. Chapter 5 introduces a novel design of light trapping transparent electrodes based on high efficiency zero-order suppression by a grating defined on top of metallic wires. The concept is demonstrated experimentally. Chapter 6 investigates the suppression of reflection losses from high-index gradient metasurfaces. This represents the first step toward using such metasurfaces as a component of transparent electrodes. Chapter 7 provides a brief conclusion and outlook.

CHAPTER 2: SIZE DEPENDENT PERFORMANCE OF LIGHT TRAPPING TRANSPARENT ELECTRODES

2.1 Introduction

[1]In the previous chapter a light-trapping transparent electrode design was introduced. The proposed design had an asymmetrical shape, leading to an asymmetrical angular response. In the present chapter we study light trapping transparent electrodes consisting of a periodic array of wires with symmetric cross-sections [53]. In order to evaluate the light trapping potential of different electrode shapes, two types of light-trapping electrodes are considered: triangular and cylindrical wire interdigitated electrodes. Figure 2.1(a) shows a conventional metallic electrode design. Light incident on the planar metallic wires is reflected, causing shadowing losses proportional to the metal areal coverage f. Figure 2.1(b) shows a light-trapping triangular metal wire electrode. In this case a large fraction of light incident on the metal wires is reflected to angles greater than the critical angle and transmitted into the substrate after total internal reflection, dramatically reducing shadowing losses. Embedded cylindrical electrodes as shown in Figure 2.1(c) also reflect a substantial portion of the incident light toward large angles and are thus expected to offer similar light trapping benefits.

---

[1] This chapter was published as Mengdi Sun and Pieter G. Kik, "Scale dependent performance of metallic light-trapping transparent electrodes," Opt. Express 28, 18112-18121 (2020)
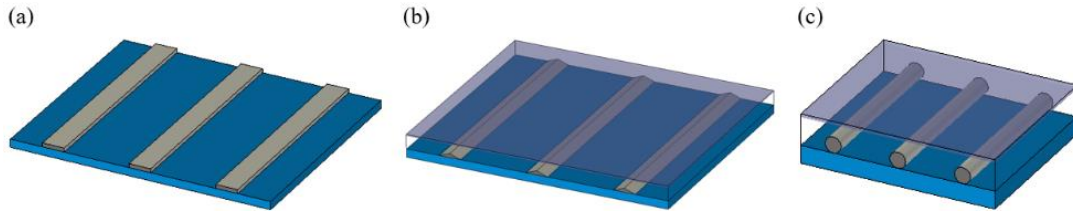
Figure 2.1: Schematics of (a) a conventional planar metallic wire electrode, (b) a triangular light-trapping metal wire electrode and (c) a light-trapping cylindrical metal wire electrode.

Figure 2.2(a) shows the simulated angular irradiance distribution of light reflected by isolated triangular silver wires with a fixed surface angle of 20° for four different widths: 200 nm, 600 nm, 1.2 μm and 2 μm. Results are shown for both TE polarization (top panel, electric field along the metal wire axis) and TM polarization (bottom panel, electric field normal to the wire axis). The results have been scaled to facilitate comparison between wires with different width.
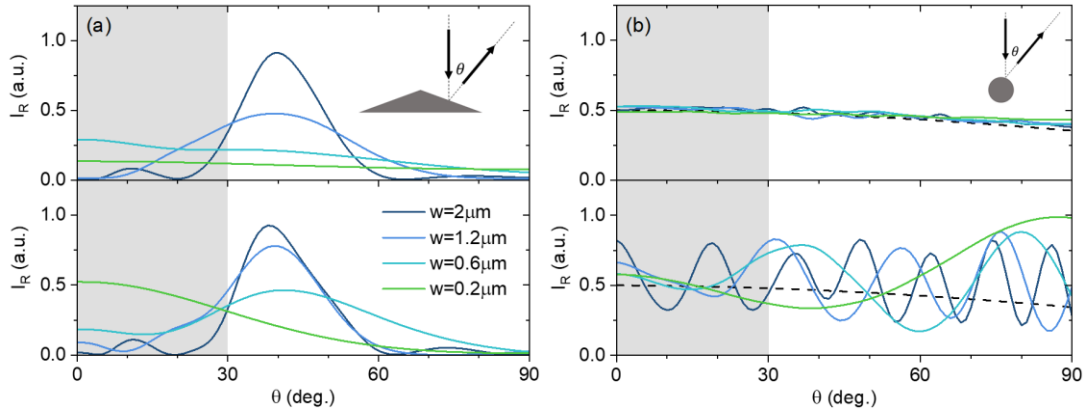
Figure 2.2: Angle dependent reflected irradiance of (a) triangular and (b) cylindrical silver wires under TE (top panels) and TM (lower panels) illumination at λ_0=750 nm for different widths *w*. The dashed lines in (b) represent the angular distributions for macroscopic silver cylinders.

Several key trends are observed. For small wire sizes, the angular distribution of the reflected light is relatively isotropic, resembling the omnidirectional radiation pattern of a line dipole. As the wire dimensions increase, the reflection becomes more directional, with reflection occurring predominantly toward angles close to 40° corresponding to the angle of specular reflection by the tilted electrode top surface. The observed angular narrowing indicates an increased light trapping potential. For example, at the chosen index of n=2 any light reflected at angles larger than 30° can be trapped using total internal reflection at a planar top surface, whereas the fraction of light reflected toward smaller angles (the gray shaded region in Figure 2.2(a)) would largely leak out of the structure. The angular distributions in Figure 2.2(a) thus predict that the light trapping performance of triangular electrodes will gradually improve as the wire width approaches ~1 μm, at which point shadowing losses may be largely mitigated. Note that off-normal

13

illumination would modify the angular distributions, which in turn will affect the light trapping performance. A detailed study of such effects is currently underway. Figure 2.2(b) shows the corresponding results for cylindrical silver wires. In contrast with the case for triangular wires, for TE illumination the angular distribution of the reflected light remains nearly isotropic for all electrode widths. For TM polarization, markedly different distributions are observed, with periodic angular patterns for all wire sizes, displaying more maxima as the wire diameter increases. These maxima result from the excitation of multipolar surface plasmon polariton (SPP) modes on the cylindrical wires, resulting in multipolar scattering patterns [54]. Note that for all cylindrical wire diameters, a significant fraction of the light is reflected toward small angle, suggesting that cylindrical wires are less suitable for optical trapping than triangular wires. At macroscopic scales, the angular distribution of reflected light under TE and TM illumination converges to a broad range of angles due to the curved nature of the reflecting surface, represented by the dashed lines in Figure 2.2(b).

2.2 Size dependent light-trapping by metal nanowire arrays

To evaluate the performance of interdigitated light-trapping electrodes, periodic wire arrays were simulated. A large metal areal coverage of f=0.25 was chosen for all structures, and the substrate and cover layer refractive index are assumed to be n=2. A 133 nm thick anti-reflective coating (ARC) with an index n=1.41 is present on the cover layer, which minimizes surface reflection for the chosen reference wavelength of 750 nm.
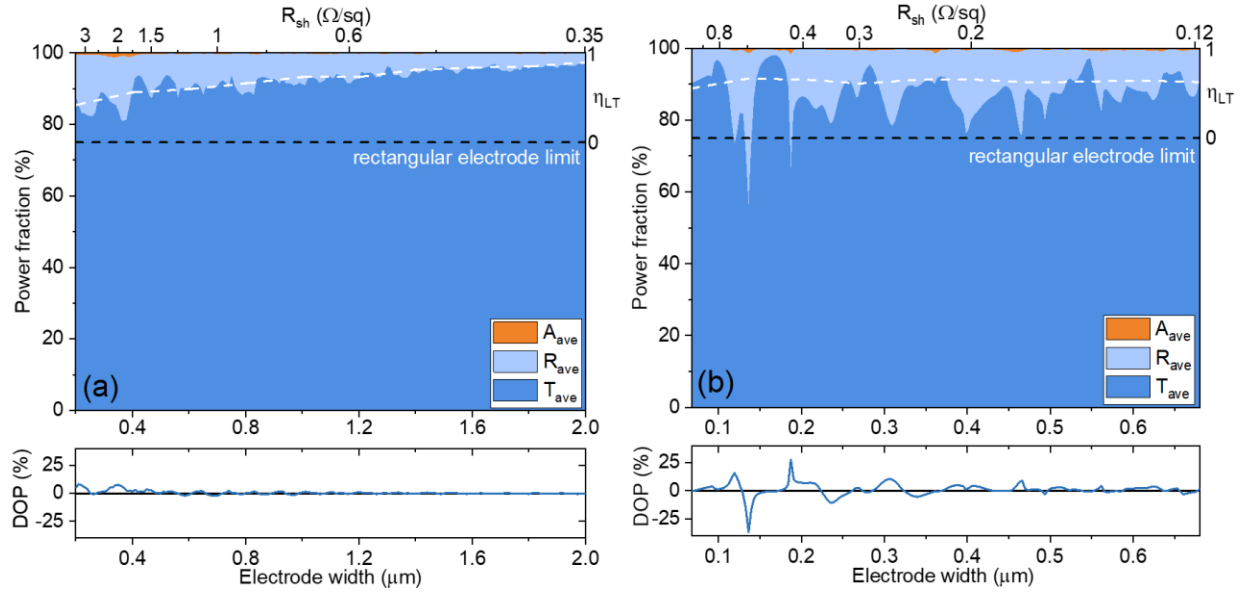
Figure 2.3: Size-dependent absorption, reflection, transmission, light-trapping efficiency η_{LT}, and sheet resistance of (a) triangular and (b) cylindrical wire arrays at 25% areal metal coverage under normal-incidence unpolarized illumination at 750 nm light (top panels) and the corresponding degree of polarization of the transmitted light (lower panels). The white dashed line represents the predicted transmission based on single-wire radiation patterns.

Figure 2.3(a) shows the simulated transmitted (T), reflected (R), and absorbed (A) power fraction of a triangular wire interdigitated light trapping electrode as a function of wire width, averaged over TE and TM polarization. For all electrode widths the transmitted fraction significantly exceeds the 75% ray optics transmission limit (horizontal black dashed line) of traditional flat electrode arrays at the simulated 25% metal coverage. Absorption loss by the metallic wires account for <1.5 percent of the incident power for all electrode sizes studied.

The corresponding degree of polarization (DOP) of the transmitted light, defined here as $(T_{TE}-T_{TM})/(T_{TE}+T_{TM})$ with T_{TE} and T_{TM} the transmitted TE and TM power fractions respectively, is shown in the lower panel. All structures exhibit a DOP magnitude below 10%, with the DOP decreasing as the electrode width increases. The corresponding effective sheet resistance for all widths is shown on the top axis. For large triangular electrodes (width w=2 μm), high optical transmittance (>97%) and extremely low sheet resistance (<0.35 Ω/sq) are achieved simultaneously. In the limit of larger ($\lambda >> \lambda_0$) electrodes, the optical performance will be affected solely by the reflection loss on the metal surfaces. Using the same literature values for the Ag dielectric response, we arrive at a transmission of T=99.88% for unpolarized incident light at λ_0=750 nm.

To quantify the light-trapping performance of the interdigitated electrode designs, we define the *light trapping efficiency* η_{LT} as the transmitted power fraction in excess of the flat electrode transmission limit, divided by the power fraction directly incident on the metal electrode lines, leading to the expression $\eta_{LT}=1-(1-T)/f$. This quantity is shown on the right axes in Figure 2.3, where the top of the transmission curve represents the quantity η_{LT}. The light trapping efficiency is seen to increase gradually from 35% to 80% as the electrode width increases from 200 nm to 2 μm. The overall trend in the transmission and light trapping efficiency can be understood by considering the angular distributions from Figure 2.2(a). For small electrode widths, a large fraction of the reflected light appears at angles smaller than the critical angle, resulting in incomplete light trapping. As the electrode width increases, the reflection becomes more directional and appears predominantly at angles beyond the critical angle (30°), resulting in

16

increased light trapping. To verify this assertion quantitatively, the white dashed line in Figure 2.3(a) shows the predicted size-dependent transmission based on the isolated-wire angular distributions in Figure 2, neglecting multiple internal reflections. The resulting curve follows the overall transmission trend remarkably well, suggesting that at this moderate metal coverage (25%) effects related to multiple reflections do not dominate the optical performance.

Figure 2.3(b) shows the corresponding results for cylindrical wire interdigitated light trapping electrode. In contrast to the results in Figure 2.3(a), cylindrical wires do not produce a gradual increase in transmittance as the wire diameter is increased, and sharp transmission reductions are observed for specific wire sizes. The lack of a rising trend in transmission is attributed to the relatively isotropic reflection distributions shown in Figure 2.2(b), causing an approximately constant reflection loss for all sizes. This is supported by the relatively constant predicted transmission (white dashed line) based on single-wire angular reflection distributions like those shown in Figure 2.2(b). The isolated wire predictions do not reproduce the observed sharp transmission minima, suggesting that these are instead related to effects involving multiple adjacent wires, e.g. grating resonances. The fact that such effects are relatively prominent in the case of cylindrical wires is also attributed to the more isotropic reflection patterns of cylindrical wires, which result in more power being radiated in the direction of adjacent wires. Note that absorption losses exceed those observed for triangular electrodes, attributed in large part to the grating-enhanced interaction of light with the lossy metallic wires. The corresponding DOP values in Figure 2.3(b) show clear peaks and dips, indicating the polarization-dependent nature of the observed grating resonances.

17

To further clarify the origin of the features observed in Figure 2.3, representative electromagnetic field distributions for periodic wire arrays with different electrode widths are shown in Figure 2.4. Figure 2.4(a) shows the electric field magnitude distribution for a triangular wire array with the largest simulated width of 2 μm under TE illumination at 750 nm corresponding to T_{TE}=96.8%, with red regions indicating large field magnitude. Fringes are observed due to the interference of the incident wave with the reflected light from the electrode, both before and after internal reflection at the cover layer surface. The narrow fringes parallel to the inclined electrode surface result from upward reflection by the metal surface. The fringes above the dielectric cover layer indicate a small degree of reflection loss. The wider fringes to the side of the metallic electrode are indicative of interference of the directly transmitted incident wave and the downward propagating recovered light that has interacted with the metallic wire. Figure 2.4(b) shows the results for triangular wires with a four times smaller width of 500 nm, shown on the same size scale, with T_{TE}=89.6%. The larger contrast in the fringes above the structure is the result of the larger reflection losses caused by the less-directional reflection from the small wires. Figure 2.4(c) shows a special case of TM-polarized light incident on a 370 nm wide triangular wire array, corresponding to the deepest transmission dip in Figure 2.3(a) with T_{TM}=74%. This electrode width is close to the silver SPP wavelength at the chosen 750 nm free-space wavelength. The transmission dip is attributed to the excitation of a standing SPP wave by the edges of the silver wire, resulting in resonantly enhanced dissipation and radiation losses. The resulting enhanced shadowing is clearly visible as the green-yellow region beneath the wires.

Figure 2.4(d) shows the field magnitude results for TM illumination of a cylindrical wire based light trapping electrode with wire width w=680 nm with T_{TM}=88%. The curved standing waves in the cover layer are indicative of a relatively isotropic reflection distribution that results in incomplete light trapping. In addition, a relatively large field intensity is observed along the metal wire circumference due to the excitation of a multipolar SPP mode. Figure 2.4(e) shows the results for a four times smaller diameter of w=170 nm under TE illumination, coincidentally corresponding to a large transmission of T_{TE}=97.2%. Note that at this size the electrode spacing is less than the free-space wavelength, preventing any high angle reflection losses under normal incidence illumination. Finally, a very sharp T_{TM} dip is observed at w=187.2 nm. To investigate the origin of this feature, panels 4(f)-(h) show the corresponding $|E|$, $|E_x|$ and $|E_z|$ distributions. Notably, the spatial period of this structure is just 0.3% below the free-space wavelength, allowing for standing waves that are weakly confined near the surface region. Inspection of the field distributions reveals a quadrupolar SPP mode on the cylindrical wires, coupled to a standing wave along the surface, similar to the process leading to Wood's anomalies. Such sharp grating resonances are suppressed in triangular wire arrays due to the more directional reflection from triangular wires.
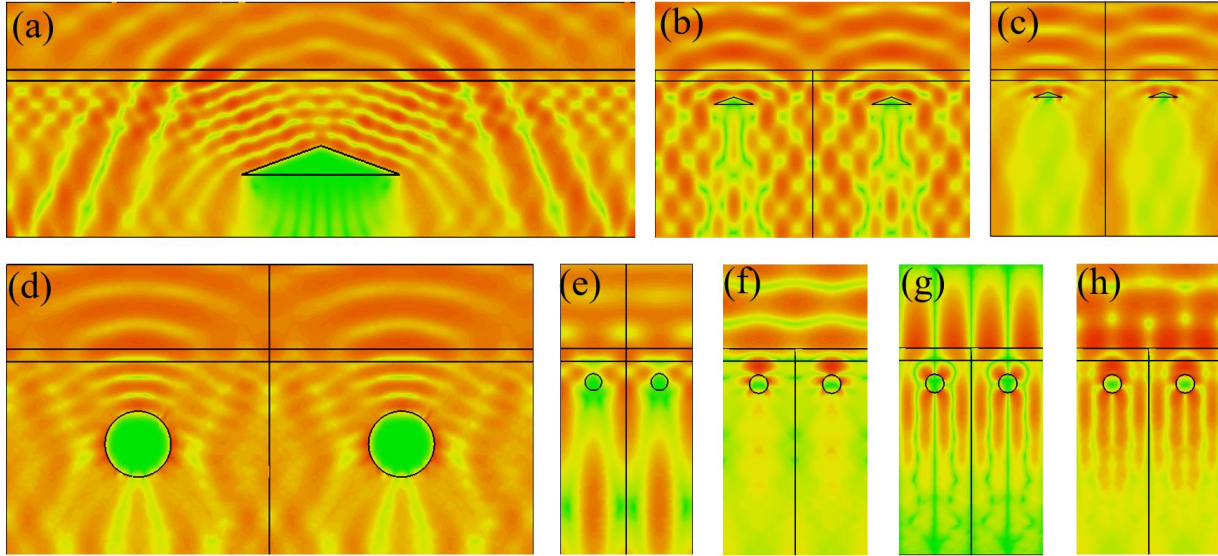
Figure 2.4: Average electromagnetic field magnitude distribution of triangular wire arrays with (a) w=2 μm and (b) w=500 nm under TE illumination, (c) w=370 nm under TM illumination, and cylindrical wire arrays with (d) w=680 nm under TM illumination, (e) w=170 nm under TE illumination, and (f)-(h) w=187.2 nm under TM illumination (E_x, E_z, and |E| contributions).

2.3 Spectral performance

The results shown thus far were achieved under fixed wavelength excitation. For optoelectronic devices such as solar cells and photodetectors, the spectral response is of critical importance. Figure 5 shows the spectral response of 2 μm wide triangular electrodes and 0.68 μm wide cylindrical electrodes both at f=0.25 for normally incident unpolarized light in the range 0.4 - 1.1 μm. The triangular wire array exhibits high transmittance (T>86%) across the entire spectrum, with T>93% from 550-900 nm. At all wavelengths, the predominant contribution to

transmission loss is reflection, with absorption losses making up only a small fraction of the total losses. A gradual spectral variation of the transmission is observed, which is attributed to the presence of the AR coating, which was optimized for 750 nm light. This is confirmed by the similar spectral shape of the transmission of the AR coating in the absence of metal wires (white dashed line). Figure 2.5(b) shows the corresponding results for the cylindrical wire light-trapping electrode. In this case, a large number of sharp transmission dips is seen, attributed to grating effects. As argued above, the prevalence of grating resonances is due to the more isotropic radiation patterns from cylindrical wires, which increases the possibility of multiple reflections on adjacent wires. Note that similar grating effects were also observed in work on mesoscale wire arrays investigated by Saive *et al* [38]. In addition to the grating-enhanced reflection losses, increased absorption due to SPP resonances is also observed at small wavelengths. As a result, the overall light-trapping performance of triangular electrodes typically exceeds that of cylindrical electrodes, providing higher transmission, reduced polarization dependence, and lower spectral variation.
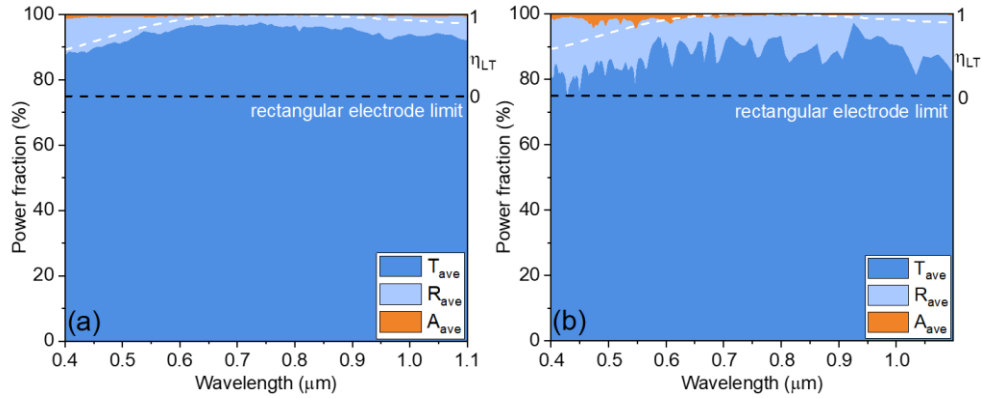
Figure 2.5: Spectral dependence of the absorption, reflection, transmission, and light-trapping efficiency η_{LT} of (a) triangular and (b) cylindrical wire arrays at 25% areal metal coverage under normal-incidence unpolarized illumination. The white dashed line represents the transmission spectrum of the AR coating in the absence of metal wires.

2.4 Figure of merit

The light trapping designs discussed above call for a new Figure of Merit (FOM) in order to compare different electrode geometries, as argued below. The performance of transparent electrodes is commonly evaluated in terms of a figure of merit (FOM) expressed as the ratio of the electrical sheet conductivity σ_s to any introduced optical loss processes [37, 55-58]. For transparent conductive films where absorption is the main source of optical loss, the FOM typically takes the form $\zeta = \sigma_s/\alpha$. In systems where shadowing contributes significantly to the optical losses, a convenient form is $\zeta = \sigma_s/(1-T)$ where the denominator now includes all optical losses including those from shadowing, and where the sheet conductivity is an effective value that takes into account the spatial distribution of the metal. However, since the effective sheet conductivity of the

light trapping systems discussed above can be increased almost arbitrarily by placing more metal directly under the wires ("in the shadow"), we propose the following light-trapping FOM to compare the performance potential of different wire shapes:

$$\zeta_{LT} = \frac{f}{1-T} \qquad (2\text{-}1)$$

This FOM captures the fact that transmission loss (factor 1-T in the denominator) is a disadvantage, whereas large metal areal coverage (*f*) is an advantage, allowing tall conductive structures to be placed on the substrate. Note that this FOM does not include statements about the exact total electrode height, but only considers the *opportunity* of placing tall electrodes in a fraction *f* of the surface. The appropriateness of this choice will be demonstrated below.

Figure 2.6 shows the introduced light-trapping figure of merit of different electrode geometries at an incident wavelength of 750 nm. The light-trapping FOM of cylindrical electrodes (blue line) is seen to be relatively unchanged as the size is increased, because of the aforementioned broad angular distribution of the reflected light from cylindrical electrodes for all electrode sizes. In contrast, the light-trapping FOM of triangular electrodes gradually improves for increasing size due to the increase in directionality of the reflected light, enabling increasingly improved transmission. For comparison, the red curve represents the predicted light-trapping FOM based on the radiation pattern of isolated triangular electrodes, taking into account analytical expressions for the angle-dependent reflection at the top surface of the structure. This simplified model reproduces the overall trend and absolute value of the ζ_{LT}. Finally, to demonstrate that the chosen form of FOM fairly evaluates the suitability of the electrode geometry for light trapping

independent of the height of the wires, we calculated ζ_{LT} for an array of 2 μm wide triangular electrodes with a 1.4 μm tall rectangular base and 2 μm wide hemicylindrical electrodes with a 1.4 μm tall rectangular base using the same numerical approach as above. The corresponding result are indicated by the square symbols in Figure 2.6. Despite the fact that this structure has an 8.6 times larger sheet conductivity, the obtained ζ_{LT} values are indeed very close to those of the triangular and cylindrical wires of the same width. This confirms that our choice of light-trapping FOM is a good measure of the light trapping efficiency of a particular electrode surface shape, while largely removing the dependence of wire height or aspect ratio.
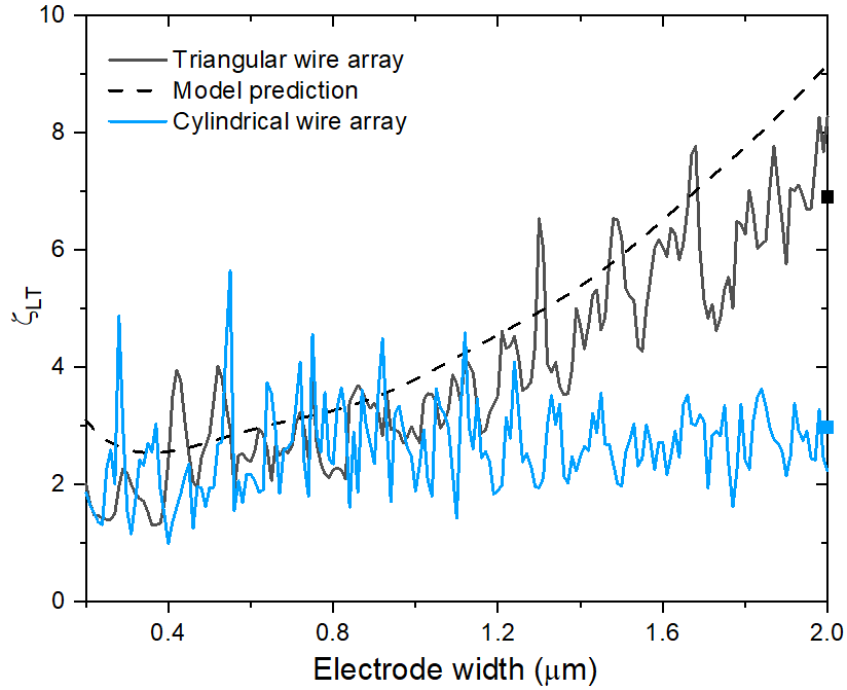
Figure 2.6: Light-trapping Figure of merit ζ_{LT} of triangular (black curve) and cylindrical (blue curve) wire arrays. The black dashed line represents a model prediction based on isolated triangular wire angular reflection distributions.

2.5 Summary

In summary, we have studied the size-dependent optical and electrical performance of triangular and cylindrical metallic wire grid light-trapping transparent electrodes. A gradual increase in optical performance of triangular wire electrodes was observed as the wire width increased. This trend was successfully explained in terms of the size-dependent angular distribution of the reflection from individual wires. Cylindrical nanowires showed no such size dependent trend, matching model predictions based on individual wire reflection distributions. The spectral response of triangular wire arrays was found to be broadband and relatively smooth,

whereas cylindrical nanowire arrays support multiple grating resonances leading to large spectral variation in transmission and a large degree of polarization of the transmitted light. All observations indicate that micron-sized triangular wire light trapping transparent electrodes substantially outperform cylindrical nanowire light trapping electrodes in terms of absolute transmission, spectral dependence, and polarization insensitivity. Triangular electrodes with a width of 2 μm and a metal coverage of 25% were found to recover as much as 88% of the unpolarized light incident on the metal portion of the wire array, resulting in 97% optical transparency and 0.35 Ω/sq. sheet resistance at a wavelength of 750 nm, with a broadband optical transmittance exceeding 86% in the wavelength range 400 nm-1.1 μm. A new figure of merit was introduced that evaluates the overall light trapping potential of transparent electrodes based on embedded shaped metallic wire arrays.

CHAPTER 3: ANGULAR DEPENDENT PERFORMANCE OF TRIANGULAR LIGHT TRAPPING ELECTRODES

3.1 Introduction

[2]In the previous chapter we studied the size dependent optical response of triangular light trapping electrodes and compared with cylindrical electrodes. The spectral response was also studied, showing high broadband transmission over the visible and near infrared spectrum. This result is vital for photovoltaic applications that involves direct sunlight illumination. An as yet unexplored aspect is the optical performance under off-normal illumination, which is also of great interest in solar cells. Based on previous discussions, it is clear that varying the external angle of incidence will affect the ray path, which could impact the efficiency of the light trapping process. In the present chapter we investigated the angular dependent optical response of triangular light trapping electrodes [59].

Figure 3.1 shows the principle of operation of the triangular light trapping electrode under off-normal illumination. Light entering the cover layer refracts toward the surface normal and either transmits through the electrode gap (cyan arrow) or is reflected upward by the metal line at a modified internal angle (blue arrows). If the upward angle is larger than the critical angle θ_c of the cover layer, the rays subsequently undergo lossless total internal reflection (TIR), redirecting the light into the substrate.
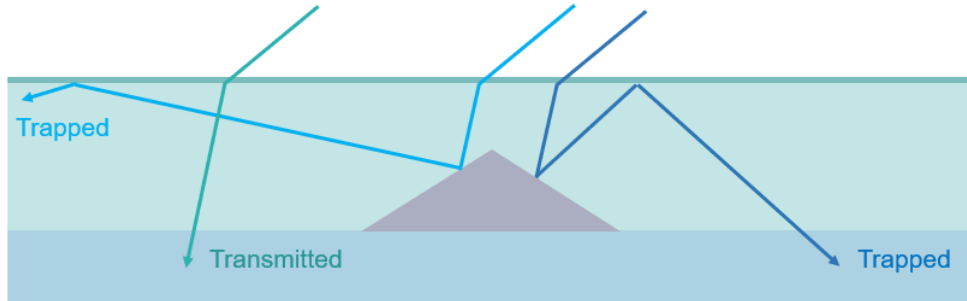
Figure 3.1: Cross section of single grid line including three example ray paths for off-normal illumination.

To study the applicability of this light trapping geometry for use over a wide angular range, the angular response of the electrode transmission will be studied as a function of three electrode parameters: the cover layer thickness, the cover layer index, and the electrode surface tilt angle. The transmission and internal field distributions are investigated using CST Studio [60] and rigorous coupled wave analysis (RCWA) [61], and the results are interpreted using a ray optics model.

3.2 Influence of cover layer thickness

We first investigate the angle-dependent transmission of an interdigitated light trapping electrode as a function of the cover layer thickness D for a metal coverage of f=25%, with a cover layer index of n_c=2.5, an electrode surface tilt angle of α_s=20°, and a metal grid line width of W=2 μm. The incident wavelength is initially chosen to be 600 nm to represent a typical visible wavelength, and the chosen ARC thickness of d_{ARC}=95 nm and index n_{ARC}=1.58 represent the optimal normal-incidence values for this wavelength. The substrate is initially assumed to be

28

index-matched to the cover layer to facilitate analysis. A similar analysis with a non-index matched substrate and broadband illumination is presented in the final section.
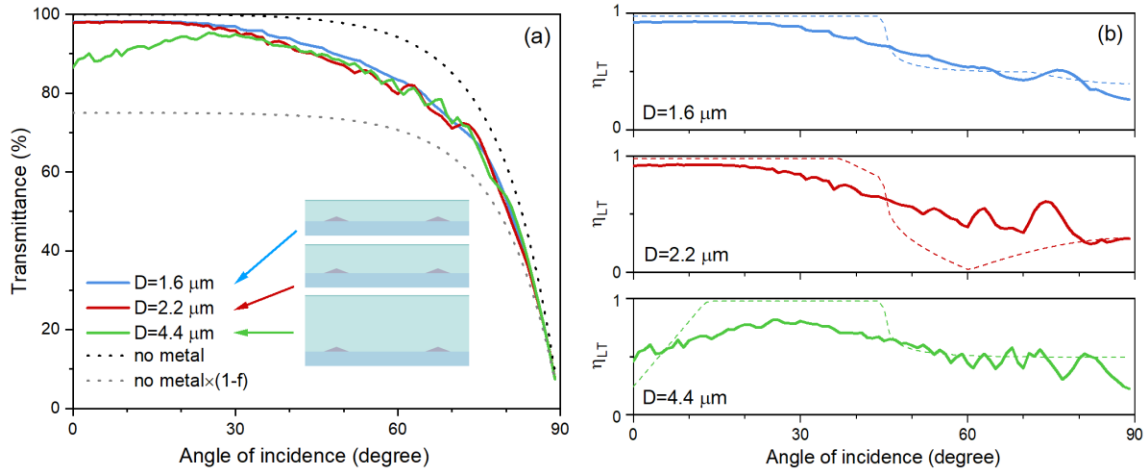
Figure 3.2: (a) Transmittance at λ_0=600 nm of light trapping electrodes with 25% metal coverage, W=2 μm, α_s=20°, n_c=2.5 three cover layer thickness values D=1.6 μm (blue), 2.2 μm (red) and 4.4 μm (green). (b) Corresponding light trapping efficiencies from numerical calculations (solid lines) and ray optics (dashed lines).

Figure 3.2(a) shows the transmission of unpolarized 600 nm light determined using RCWA as a function of external angle of incidence θ for cover layer thickness values D of 1.6 μm, 2.2 μm, and 4.4 μm, where D is the distance from the base of the grid line to the bottom of the ARC layer. Note that two of the curves show transmission values as high as 98% for near-normal incidence illumination, despite the fact that the sample has only 75% open area. This demonstrates near complete recovery of shadowing losses through light trapping.

All three curves show a gradual drop in transmission as the external angle of incidence is increased. For comparison, the black dotted line shows the analytically calculated transmission of

unpolarized light through the same structure in the absence of metallic lines. This curve, which we will call $T_{max}(\theta)$ sets an upper limit to the transmission, accounting for reduced transmission at high angle due to increased top surface reflection loss. The gray dotted line shows the related quantity $T_{min}(\theta)=(1-f)\cdot T_{max}(\theta)$, which represents the expected transmission in the absence of any light trapping. For cover layer thickness values of 1.6 μm and 2.2 μm the low-angle transmission lies remarkably close to the upper limit of the transmission, indicating very efficient light trapping. As the incident angle is increased, the transmission curves deviate from the calculated upper limit, but stay well above the expected transmission in the absence of light trapping.

To analyze the optical performance of the transparent electrode we introduce the light trapping efficiency η_{LT}, defined as $\eta_{LT}=(T-T_{min})/(T_{max}-T_{min})$. The denominator which is equal to $f\cdot T_{max}$ represents the fraction of light incident on metal that may be recovered via light trapping, while the numerator represents the actual fraction of light that was recovered. Defined this way, η_{LT} is equivalent to the reduction in shadowing losses. The corresponding light trapping efficiencies for the three geometries from Figure 3.2(a) are shown in Figure 3.2(b) (solid lines). For electrodes with D=1.6 μm and 2.2 μm, the light trapping efficiency is close to 100% at small angles, indicating that a large fraction of light incident on the metal is reflected upward at angles larger than the critical angle followed by total internal reflection and transmission into the substrate. As the external angle of incidence is increased, the light trapping efficiency drops gradually, reaching a value of ~25% at glancing angle illumination (θ=90°). In contrast, the electrode with D=4.4 μm shows a relatively low light trapping efficiency of ~50% at normal incidence that briefly rises to ~75% followed by a gradual drop towards higher angles.

30

To understand the trends observed in Figure 3.2(b) a simplified ray optics model was developed where any ray that encounters a metal surface twice is considered lost. Reflection losses at the metal surfaces and partial internal reflection at the top surface are taken into account. The corresponding predicted transmission results are included in Figure 3.2(b) as dashed lines. For all three cases the ray optics model predicts a relatively sudden drop in the light trapping efficiency at $\theta = 44°$. This can be understood by considering the critical angle of the cover layer. As the external angle of incidence is increased to positive angles (to the right side of the surface normal), the internal refracted angle increases correspondingly according to Snell's law. This in turn *increases* the angle of the upward ray generated by the left half of the grid line (light blue ray Figure 3.1) while *decreasing* the angle of the upward ray generated by the right half of the line (dark blue ray in Figure 3.1). As the incident angle reaches $\theta = 44°$ the angle of the latter ray drops below the critical angle of the cover layer, causing a loss of TIR and precluding efficient light trapping. A very subtle additional efficiency drop is seen to start at $\theta = 72°$, which corresponds to the angle at which the left ray impinges on a neighboring grid line, a loss process which we will call secondary shadowing. At a larger cover layer thickness (D=2.2 μm) the same internally reflected ray travels further before reaching the substrate, and consequently secondary shadowing occurs at a smaller angle of incidence of 38°. At D=4.4 μm, secondary shadowing is already present under normal incidence illumination, leading to the relatively low light trapping at small angles.

Comparing the numerical results with the ray optics results in Figure 3.2(b) it is evident that the numerically predicted loss of light trapping occurs over a broader angular range than

31

expected from ray optics. This is attributed to diffractive effects: the upward reflected light is generated by a relatively narrow grid line, which introduces significant angular spread in the reflected beam [53]. A second key difference is the near-absence of any evidence of secondary shadowing in the numerical data, which is also attributed to diffractive effects. The angular spread of the reflected beams results in a distance dependent width of the reflected beam that increasingly exceeds the adjacent wire width at larger propagation distance. Consequently, only a small fraction of the internally reflected light interacts with an adjacent wire at any given angle of incidence.
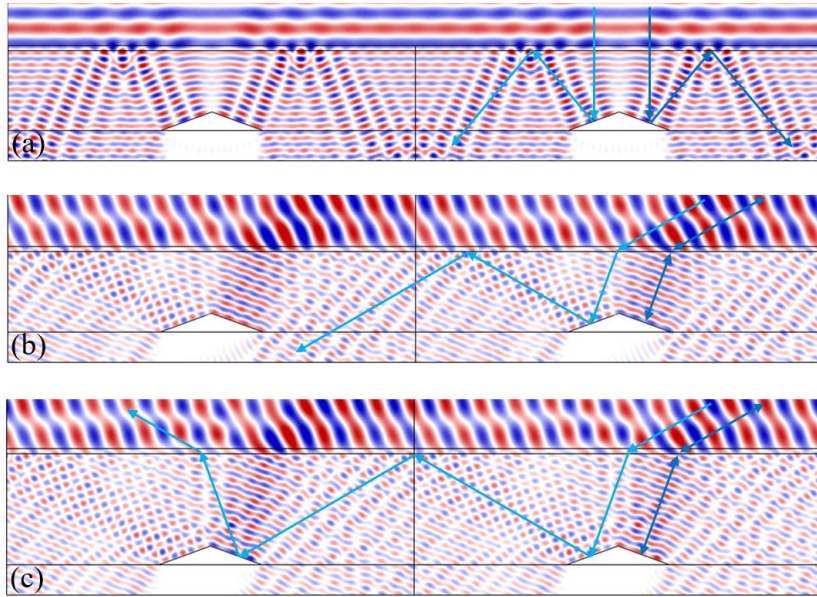
Figure 3.3: TE field distributions of 2 μm wide light trapping electrodes in n_c=2.5 at 25% metal coverage with surface tilt α_s=20° for (a) θ=0° and D=1.6 μm, (b) θ=60° and D=1.6 μm and (c) θ=60° and D=2.2 μm.

Figure 3.3 shows numerically simulated TE (s-polarized) field distributions around silver light trapping electrodes under 600 nm illumination, corresponding to key scenarios discussed

above. The wave propagation direction is indicated by the arrows. Figure 3.3(a) shows the case of near-complete light trapping under normal incidence illumination. Note that while a shadow is present under the wire as evidenced by a lack of wavefronts, there is very little loss of transmission due to the fact that this missing light is recovered by TIR. Figure 3.3(b) demonstrates that at large external angle of incidence, part of the light incident on the metal grid line is reflected upward at relatively small internal angle. This is indirectly visible as the standing wave pattern above the right half of the grid lines. The reflected light travels upward at an angle below the critical angle, resulting in large transmission back into air, reducing the overall transmission (dark blue arrows). Figure 3.3(c) shows the field distribution for the same angle of incidence as in Figure 3.3(b) but with a larger cover layer thickness of $D=2.2$ μm, which can introduce secondary shadowing due to an additional radiative loss pathway (light blue arrows).

3.3 Influence of cover layer index

The preceding section demonstrated that the light trapping efficiency drops significantly when light is reflected at upward angles below the critical angle, causing a loss of TIR. Since the internal angle is affected by the refractive index of the cover layer, the angular performance of light trapping electrodes is expected to depend critically on the refractive index of the cover layer. To evaluate this aspect, we investigate the angular response of the electrodes for three values of the cover layer index: $n_c=1.5$ representative of glass ($\theta_c=41.8°$), $n_c=2.2$ representative of e.g. aluminum nitride ($\theta_c=27°$) and $n_c=4$ representative of e.g. silicon ($\theta_c=14.5°$). The geometry is kept

fixed with f=0.25, α_s=15°, W=2 μm, and D=1 μm as shown in the inset of Figure 3.4(a). The small

cover layer thickness was chosen to minimize the risk of secondary shadowing.
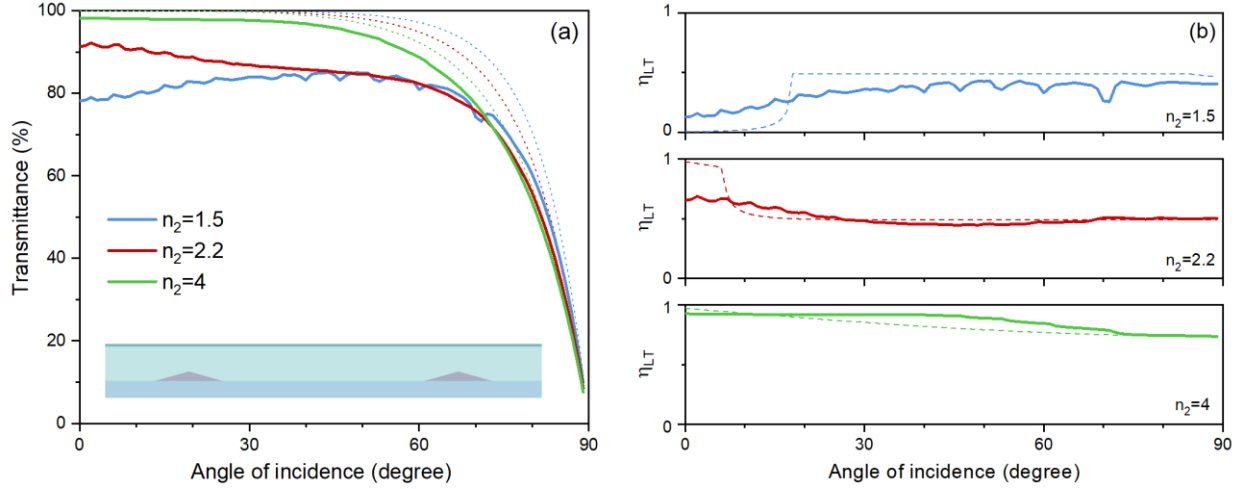
Figure 3.4: (a) Transmittance of light trapping electrodes with f=0.25, W=2 μm, D=1 μm, α_s=15° for three different cover index values n_c=1.5 (blue), 2.2 (red) and 4 (black). The dotted lines represent transmission in the absence of metal. (b) Corresponding light trapping efficiencies from numerical calculations (solid lines) and ray optics (dashed lines).

Figure 3.4(a) shows the calculated angle-dependent transmission for the three choices of

cover layer index. Similar to the observations in Figure 3.2, all transmission curves drop steeply

at high angle of incidence which is predominantly due to top surface reflection losses. This is

confirmed by the $T_{max}(\theta)$ curves, representing the same structures without metal (dotted lines).

Note that all curves show a small-angle transmission larger than 75% with f=0.25, indicating that

some degree of light trapping is achieved in all three cases. For incident angles below 45° the

higher index cover layers are seen to yield larger optical transmission.

Figure 3.4(b) shows the corresponding light trapping efficiency curves (solid lines) from numerical calculations and based on the previously discussed ray optics model (dashed lines). For a cover layer index of n_c=1.5 (blue line) the numerically determined light trapping efficiency at normal incidence is low (~12.8%), and near-zero according to the ray optics model. This is due to the fact that TIR is not achieved for these parameter choices. Under normal incidence illumination, the upward rays appear at an angle of 30° (twice the surface tilt, independent of refractive index) which is below the critical angle of 42° at this index, resulting in transmission of the reflected rays back into air. This case is illustrated for TE illumination in Figure 3.5(a). Note the significant lateral variation of the electric field strength outside the electrode structure, indicative of interference of the incident plane wave and high-angle light exiting the structure. As the angle of incidence is increased, the angle of the left upward ray increases, leading to the onset of light recovery through TIR at an incident angle of 18°. TIR is not achieved for the right ray at any positive external angle. An example field distribution for this scenario is shown in Figure 3.5(b) for θ=30°. The lack of TIR for light incident on the right side of the grid line results in the observed upper limit of 50% light trapping efficiency in the top panel of Figure 3.4(b).

For intermediate cover layer index (n_c=2.2) the normal incidence light trapping efficiency starts at ~65.5% and drops gradually to ~50% as the incident angle is increased. The ray optics model clarifies these observations: at normal incidence, the reflected rays again appear at 30° which in this case is above the critical angle of θ_c=27° for this refractive index. While this in principle this would allow for efficient light trapping, the angular spread of the reflected beam due to the previously discussed diffractive effects leads to significant radiative losses. As the incident

angle is increased beyond $\theta=12°$, TIR is lost for the right upward ray, resulting in a lower light trapping efficiency of ~50%.

Remarkably, when using a large cover layer index ($n_c=4$) the simulated light trapping efficiency exceeds 73% for all incident angles and is above 85% over a 120° angular range. This large suppression of shadowing loss over such a wide angular range is the result of two related effects. First, the high index causes strong refraction as the light enters the cover layer, and consequently the light is incident on the grid line at near-normal incidence even for large external angles. Second, due to the small critical angle of $\theta_c=14.5°$, light trapping is achieved even at small internal angles. Figure 3.5(c) shows the corresponding TE field distribution for normal incidence illumination. Note the absence of lateral variation of the external wavefronts, indicative of efficient light trapping. Figure 3.5(d) shows the same structure for 30° angle of incidence. Note that even though the incident angle increased significantly, the changes in the internal ray paths compared to Figure 3.5(c) are relatively small due to the strong refraction, and thus trapping remains efficient. The external wavefronts remain approximately planar even at this large angle of incidence, indicative of small surface reflection and efficient light trapping.
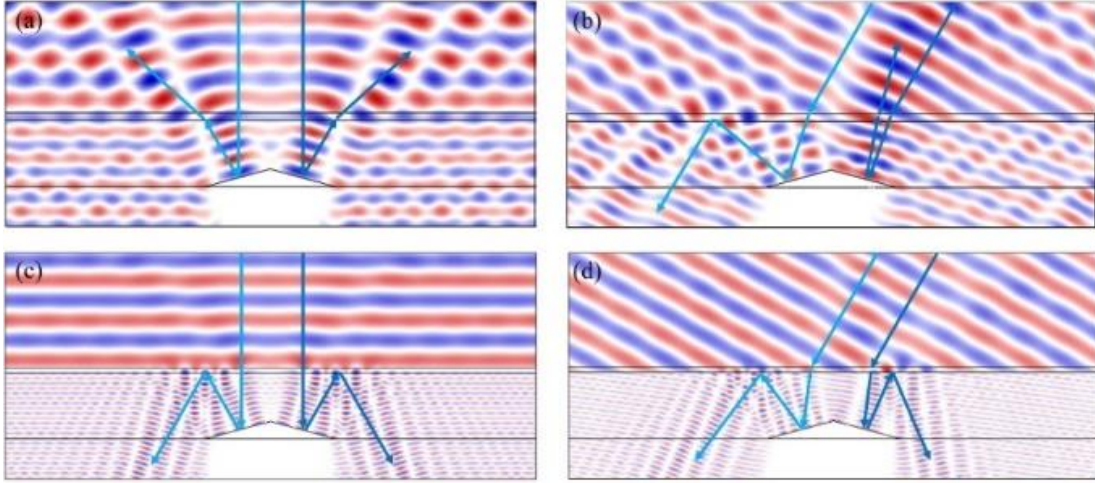
Figure 3.5: TE field distributions of light trapping electrodes with *f*=0.25, W=2 μm, *α*ₛ=15°, *D*=1 μm for a cover layer index of *n_c*=1.5 at (a) normal incidence and at (b) 30° angle of incidence, and for a cover layer index of *n_c*=4 at (c) normal incidence and (d) 30° angle of incidence.

3.4 Influence of surface tilt angle

In the preceding section, it was observed that normal incidence illumination for n_c=1.5 and α_s=15° TIR was not achieved, resulting in low light-trapping efficiency. This problem can be mitigated by using larger surface tilt. In the following we evaluate the light trapping performance for three surface tilt angles: α_s=0°, 15°, and 30°. The remaining parameters are held fixed at f=0.25, n_c=1.5, W=2 μm, and D=1 μm.
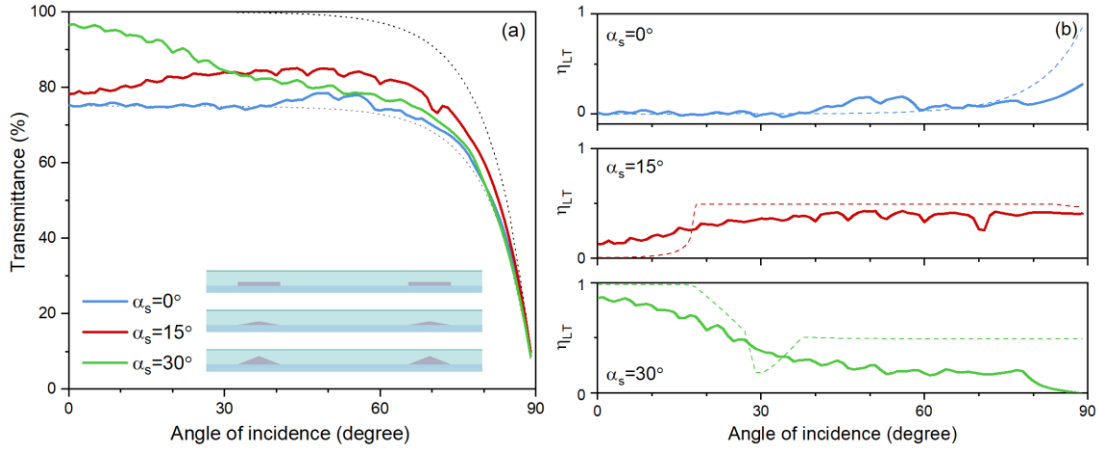
Figure 3.6: (a) Transmittance of light trapping electrodes with *f*=0.25, W=2 μm, *n_c*=1.5, and D=1 μm for surface tilt angles *α_s*=0° (blue), 15° (red) and 30° (green). (b) Corresponding light trapping efficiencies from numerical calculations (solid lines) and ray optics (dashed lines).

Figure 3.6(a) shows the simulated angle-dependent transmittance for all three choices of surface angle. As before, the loss of transmission at high angle is largely due to top-surface reflection, and all curves lie almost entirely between the estimated maximum (perfect light trapping, black dotted line) and minimum transmittance (zero light trapping, gray dotted line) curves. Figure 3.6(b) shows the corresponding light trapping efficiency curves, as well as the predicted light trapping efficiency based on ray tracing. The top panel shows the results for flat embedded electrodes, similar to standard flat top electrodes on silicon solar cells. As expected, flat electrodes exhibit near zero trapping efficiency at small angles. A distribution of the TE field magnitude for an incident angle of θ=30° is shown in Figure 3.7(a), along with the propagation direction indicated schematically by the white arrows. Note the bright standing wave pattern above

38

the grid line and outside the structure, showing that light trapping is largely absent. To highlight the importance of light trapping we compare the performance of triangular wires with a flat-wire electrode. Note that a commonly used dome-shaped wire would outperform a flat electrode due to some degree of forward scattering by the inclined wire sides [53, 62, 63]. The case of intermediate surface angle (middle panel in Figure 3.6(b)) is identical to a previously shown result (top panel in Figure 3.4(b)), revealing the previously discussed onset of partial light trapping for an incident angle of 18°. The lower panel shows the light trapping efficiency for a large electrode surface tilt angle of $\alpha_s=30°$. In this case the near-normal incidence results show ~85% light trapping efficiency even with this low cover layer index. This value is lower than the prediction from the ray optics model (nearly 100%) because of diffractive effects, causing some of the reflected light to propagate at an angle below the critical angle. At an external angle of 18° the ray optics model predicts the onset of secondary shadowing, followed by loss of TIR at 28° and recovery of secondary shadowing as some of the reflected light passes over the next grid line. These effects cannot be clearly distinguished in the simulated data due to diffractive effects. The TE field magnitude distribution for normal incidence illumination is shown in Figure 3.7(b). Note that zero reflection loss would produce a homogeneous field magnitude above the cover layer. The fact that a faint standing wave pattern is visible indicates the presence of some reflection loss due to a combination of diffractive effects and interactions with adjacent grid lines. Despite this small reflection loss, a total normal incidence transmission of 96% is achieved at 25% metal areal coverage.
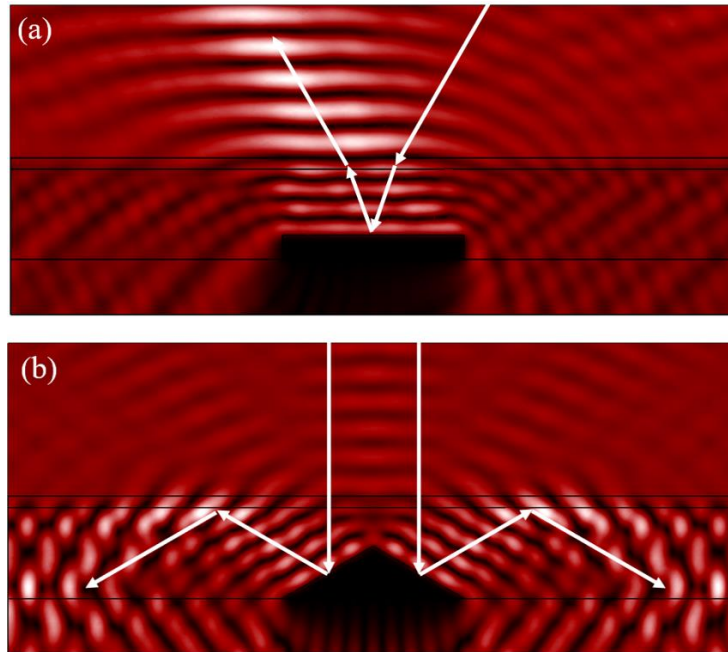
Figure 3.7: TE field magnitude distributions for λ_0=600 nm, f=0.25, W=2 μm, D=1 μm and n_c=1.5 for surface tilt angles of (a) α_s=0° at 30° angle of incidence and (b) a surface tilt of α_s=30° at normal incidence.

3.5 Device performance using real material properties

Figure 3.8 summarizes the main identified contributions to non-ideal optical transmission in interdigitated light trapping electrodes. First, any light incident at high angle will experience some top surface reflection loss (dashed cyan ray) even in the presence of an anti-reflective coating (ARC). This type of loss is also incurred in e.g. commercial encapsulated silicon solar cells. Second, for off-normal illumination, internally reflected light may propagate at an angle below the critical angle, resulting in a loss of TIR (dark blue ray). Finally, at large incident angle and small

40

wire spacing, internally reflected light may impinge on an adjacent electrode, potentially leading to dissipation or escape from the light trapping structure (light blue ray). These effects can be mitigated by using a large cover layer index, a large surface tilt, a large wire spacing, and small cover layer thickness.
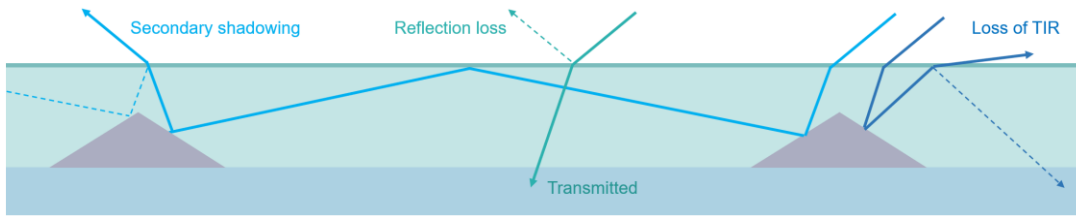
Figure 3.8: Key optical loss mechanisms total transmission and light trapping efficiency. Dashed lines indicate relatively weak contributions. The cover layer and substrate are assumed to be index matched in this schematic.

Given the challenges discussed above, it is of interest to evaluate the complete spectrally dependent performance of a system that more closely resembles a real-world device, for example an encapsulated silicon solar cell. Unlike the assumptions in the preceding discussions, here we consider a realistic index mismatch between the cover layer and the substrate. To represent a typical Si solar cell, we assume a glass cover layer [64, 65] which has an index similar to typical encapsulation materials. The substate is represented by lossless but dispersive silicon [66]. An ARC consisting of MgF_2 [67] with a thickness of 109 nm is used at the top surface, and an AlN [68] ARC is placed at the glass-silicon interface (62.5 nm thickness, n=2.2). The cover layer thickness is set to D=1.1 μm, the metal coverage is set to f=0.1 with an electrode width W=2 μm and a surface angle of α_s=30°.

Figure 3.9(a) shows a schematic of a single grid line in the simulated structure. Figure 3.9(b) shows the angle dependent reflection spectrum for this structure at f=0.1. The large reflection losses at short wavelength are largely due to top surface reflection, due to the non-ideal AR response of the thin MgF_2 layer at short wavelengths. Figure 3.9(c) shows the corresponding light trapping efficiency spectra. Note that at angles up to 30° shadowing losses are reduced by more than a factor two for all wavelengths (colors yellow through green). The spectrally averaged shadowing reduction over a wide angular range (-60° to 60°) under AM1.5 solar irradiation [69] is 56.1%. The simulated structure shows a nearly polarization-independent spectrally averaged optical transmission of T=90.2% (T_{TE}=89.8% and T_{TM}=90.7%). These results demonstrate that even in a challenging real-world situation with large index mismatch between substrate and cover layer, shadowing losses can be reduced by more than a factor two over a wide angular and spectral range using compact light trapping electrodes. The effective sheet resistance of this structure is R_{sh}=0.22 Ω/sq, far below typical industrial requirements (R_{sh}<100 Ω/sq) [70, 71], demonstrating the unique possibility of simultaneously achieving low shadowing losses and high electrical conductivity.
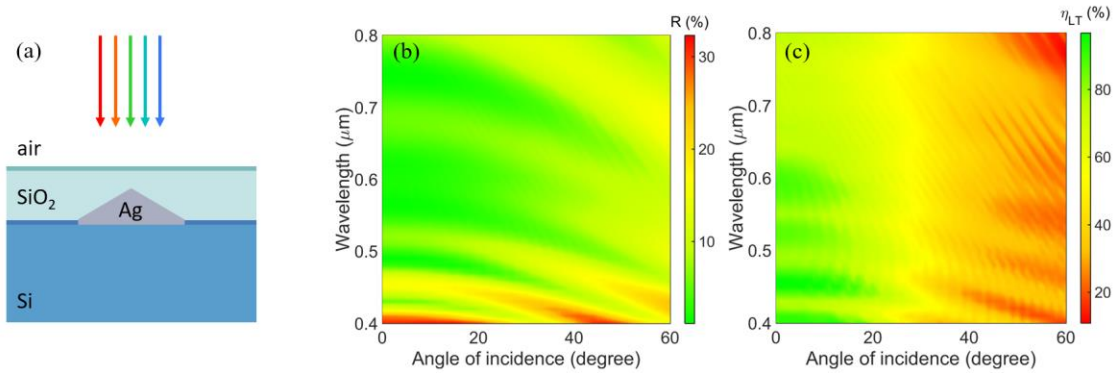
Figure 3.9: (a) Schematic of a light trapping transparent silver electrode on an encapsulated silicon solar cell. (b) Reflectance and (c) light trapping efficiency of an encapsulated Si solar cell with f=0.1, W=2 μm, D=1.1 μm and α_s=30°.

3.6 Summary

In summary, the angle dependent optical response of triangular light trapping electrodes was investigated numerically and analytically. A ray optics model was developed to predict the transmission of light trapping electrodes. Three effects that adversely affect light trapping were identified: partial loss of TIR at large angle of incidence and the absorptive and radiative loss due interaction with the neighboring electrodes (secondary shadowing). Additionally, the light trapping performance was evaluated in terms of the light trapping efficiency that represents the reduction of shadowing losses. The influences of surface tilt angle, cover layer thickness and cover layer index on the light trapping efficiency were investigated. Electrodes with higher cover layer index, larger tilt angle and smaller cover layer thickness were found to enable high light trapping efficiency. Using realistic material properties it was found that shadowing losses in a silicon solar

cell with 10% metal coverage and an effective sheet resistance of 0.22 Ω/sq can be reduced by

56% averaged over a 120° angular range and spectrally averaged over the AM1.5 solar spectrum.

CHAPTER 4: EXPERIMENTAL DEMONSTRATION OF LIGHT-TRAPPING TRANSPARENT ELECTRODES

4.1 Introduction

In previous chapters we numerically investigated the size and angular dependent optical response of triangular light-trapping electrodes and discussed their potential use in optoelectronic devices such as photovoltaic devices and high-speed photodetectors. The simulations indicated that shadowing by metallic contacts could be drastically reduced for specific wire geometries. In the present chapter we experimentally investigate prototype light-trapping transparent electrodes fabricated by multi-photon lithography and selective chemical deposition. The electrodes consist of nanowires with tilted metallic surfaces embedded in a dielectric cover layer. Light incident on the metallic contacts is recovered by total internal reflection to eliminate the shadowing losses. The light trapping efficiency is studied as a function of surface inclination. Dark-field microscopy studies indicate that significant light trapping is achieved for electrodes with surface tilt angles equal to or larger than 25°, and laser scanning is used to corroborate these findings. It is demonstrated that at 30° surface tilt, near 60% light trapping efficiency is achieved.

4.2 Prototype fabrication

The prototype electrodes were fabricated on a glass substrate using multi-photon lithography. In brief, the output of a femto-second mode-locked Ti-Sapphire laser was focused through a high-NA objective lens into a commercial acrylic resin, IP-DIP, to induce multi-photon polymerization. Using a three-axis nano-positioner, the focal volume was controllably positioned

with respect to the substrate to define the 3D pattern. The exposed 3D volume determines the shape of the eventual prototype electrode. To reduce the fabrication time, a contour-writing method [72] was used for defining the electrodes. The unpolymerized IP-DIP resin was washed thrice with propylene glycol monomethyl ether acetate (30 minutes each) and once with IPA (15 mins) to develop the microstructure. The sample was immersed in isopropanol and UV-flooded (Loctite Zeta 7411-S) for 10 minutes to polymerize the exposed volume, which will form the core of the metallized wire, and subsequently rinsed with isopropanol and dried in air.

The fabricated structures were metallized through selective deposition using a modified literature procedure [73-75]. The polymeric microstructures where washed with N,N-dimethylformamide and immersed in an ethanoic solution of ethylene diamine (20 vol.-%) for two hours. Amines react selectively with the unreacted acrylic groups of the polymer through Michael addition, leaving behind pendant amine groups on the surface. The sample was washed thoroughly with ethanol and DI water. The substrate was then immersed in chloroauric acid (0.53 mM in water) for two hours to immobilize Au^{3+} ions by coordination to the aminated surface, then washed with DI water and immersed in a solution of sodium borohydride (0.1 M in water) to form surface-bound gold nanoparticles (AuNPs) [76]. Importantly, the substrate was then rinsed with dilute HNO_3 (1 wt.-% in water) to wash away any unbound AuNPs. AuNPs-primed surface was used for electroless copper enhancement [74] to create reflective electrode surfaces. The substrate was immersed in a bath of Cu^{2+} (copper sulfate 1.5 wt.-%, sodium hydroxide 2 wt.-%, and sodium potassium tartrate 7 wt.-% in DI water) for 25 mins, washed with copious DI water, and dried in air. The final structure is representative of surface shaped metallic wires, with the shape of the wire determined by the polymer core, and the metal wire surface represented by the thin Cu layer.

4.3 Device characterization by scanning electron microscopy

Figure 4.1(a) schematically shows the design for the fabrication, including wires with a length of 50 μm, a width of 14 μm, and peak thickness of 6 μm, and a surface tilt angle that is varied linearly from 0-30° with an increment of 5°. The wires are spaced closely together to simplify optical analysis. Figure 4.1(b) shows a scanning electron microscopy (SEM) image the as-fabricated dielectric wires on a glass substrate. Note that the design geometry is well-replicated in the developed polymer. Subsequently the exposed wire surfaces were selectively metallized by electroless copper deposition. The conformal chemical deposition used in this work enables arbitrary spacing between the electrodes, in contrast to oblique angle deposition methods which are based on shadowing [77, 78]. Figure 4.1(c) shows an SEM image of the metallized electrodes. Note that the metallization process does not affect the wire geometry (size, shape and tilt angle). A magnified perspective view of a single model electrode is shown in Figure 4.1(d), demonstrating the selectivity of deposition. The surface of the electrode appears rough due to the morphology of deposited copper nanoparticles [74] whereas the glass surface remains smooth after metallization. Energy dispersive X-ray spectroscopy (EDS) measurements confirmed the selective deposition of copper on the electrodes (Figure C.1 in Appendix C).
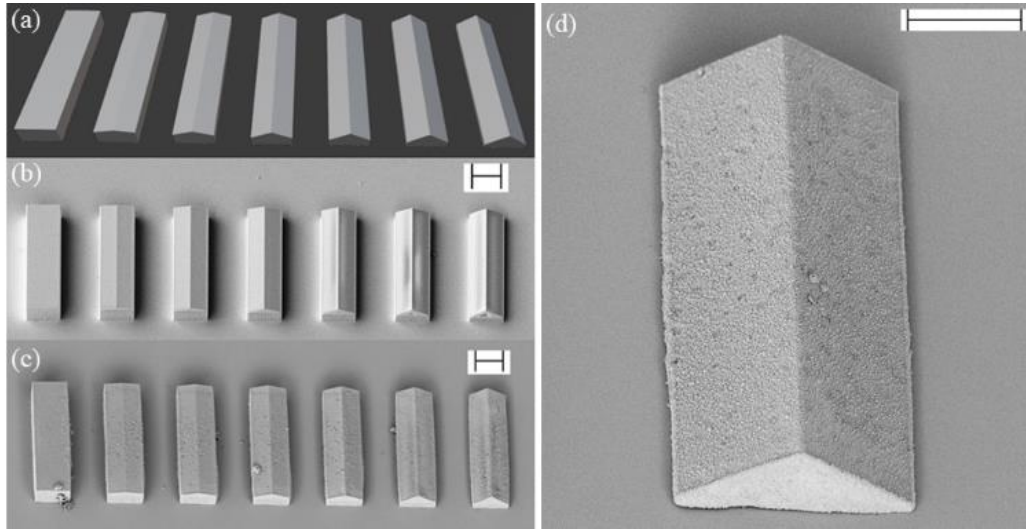
Figure 4.1: Prototype light-trapping electrodes with surface angles ranging from 0-30°. (a) Model design, (b) SEM image of the fabricated sample before and (c) after metallization. (d) High-magnification view of a single electrode a 30° surface tilt. All scale bars correspond to 10 μm.

4.4 Device characterization by optical microscopy

Metallized prototype light trapping electrodes were investigated using optical microscopy. Figure 4.2(a) shows a bright-field reflection microscopy image of an as-fabricated array of metallized wires with a length of 50 µm, a width of 12 µm, and a height of 6 µm in the absence of a cover layer, as well as a schematic of the measurement geometry. The leftmost and rightmost wires have zero surface tilt, while the surface tilt angle of the remaining six wires varies from 10° to 35° in steps of 5° from left to right. An objective lens with 50× magnification and a numerical aperture of NA=0.8 was used, corresponding to a maximum collection angle of 53°. The illumination was carried out with a small aperture stop, ensuring near-normal illumination

spanning a small angular range from -15° to 15°. It is shown that metallized wires with surface angles in the angle from 0 - 20° appear bright in reflection mode and those with tilt angles ≥25° gradually become dark. This observation is not the result of light trapping, but rather due to redirection of the incident light to angles beyond the collection N.A. of the objective. For example, normal incidence illumination of a wire with a surface tilt angle of 25° results in a 50° reflected angle, close to the maximum collection angle of the objective. The reduced collection efficiency of the reflected light results in a dark appearance of wires with large surface inclination. Note that the surrounding area appears relatively dark due to the low reflectance of the glass substrate. Relatively high surface roughness is observed for the wires, which matches the morphology shown in Figure 4.1(d).
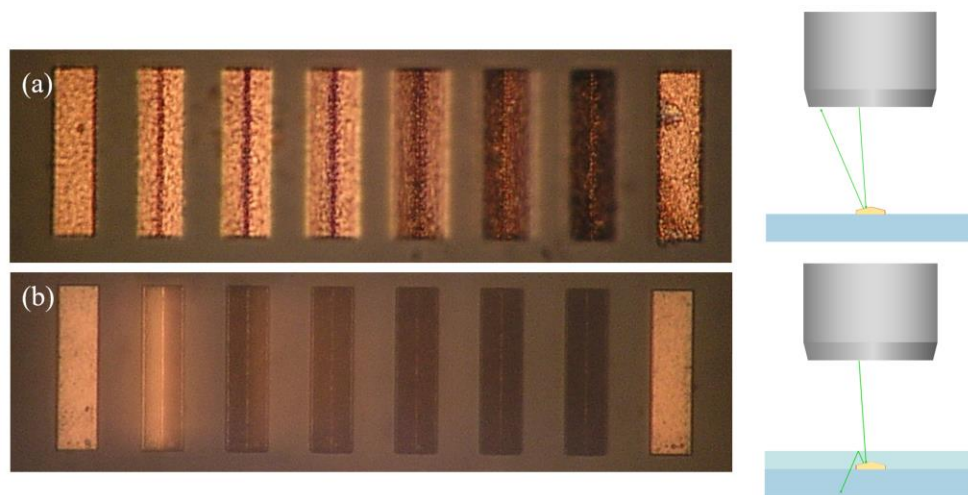
Figure 4.2: Reflection microscopy image and measurement schematic of (a) uncovered metallized and (b) covered metallized light-trapping electrodes.

To mimic the light-trapping geometry a drop of index-matching liquid (n=1.518) is placed on the sample, and a microscope cover slip is placed on top. The cover slip and index-matching

liquid together take the role of the cover layer, resulting in a critical angle of θ_c=41.2°. Under normal incidence illumination, light trapping is therefore expected for electrodes with a surface tilt in excess of 20.6° corresponding to the two rightmost tilted wires in Figure 4.2. Figure 4.2(b) shows the brightfield reflection image and a measurement schematic of the sample in the light trapping configuration. In the light-trapping measurement geometry the leftmost and rightmost wires with 0° tilt still appear bright due to a lack of light trapping, corresponding to a significant portion of the shadowing losses from these wires. The brightness of the wire images decreases significantly for electrodes with high surface tilt. The third (15° tilt) and fourth (20° tilt) wires already show reduced brightness despite the fact that the internal reflected angles at normal incidence illumination of 30° and 40° respectively are smaller than the critical angle (θ_c=41.2°). This observation is attributed to the fact that the upward reflected light strongly refracts at the sample surface, leading to angles that are close to or larger than the maximum collection angle of the microscope objective. Assuming perfect normal incidence illumination, the surface angles of 15° and 20° would produce external angles of 49° and 75°, compared to a maximum collection angle of 53°. Taking into account the nonzero beam spread (approximately 30° angular spread about the normal), a significant fraction of refracted light is not collected, even for the wire with 15° surface tilt, resulting in a dark appearance. The fifth (25° tilt), sixth (30° tilt) and seventh (35° tilt) wires appear largely dark, which is attributed to successful trapping of reflected light. The edges of the structure remain visible in the image, which is attributed to the fact that sharp edges scatter light into a wide range of angles, some of which will appear below the critical angle, contributing to the image formation. Furthermore, the surface roughness of the wires appears

reduced for the covered sample, which is attributed to a reduction in image quality due to the additional refraction introduced at the cover slip surface.

4.5 Device characterization by linear laser scanning

While the microscopy analysis in Figure 4.2 strongly suggests light trapping due to the reduction in the amount of reflected light collected from the sample in brightfield reflection microscopy, the trapped light itself was not detected. This could lead to an overestimation of the light trapping performance, since any light exiting the structure at angles beyond the maximum collection angle of the objective would not be visualized, but would still constitute shadowing losses. To eliminate this source of uncertainty, we investigate light trapping of the transparent electrode design by measuring the on-axis and off-axis transmitted optical power under normal-incidence illumination of isolated metallized wires. A sample containing well-separated wires with a length of 100 µm, a width of 20 µm, a height of 5.77 µm, and a surface tilt of 30° with index matching oil and cover slip applied was placed on top of a dove prism. In order to detect the trapped light, index matching oil was applied between the sample and the prism, allowing trapped light to transmit into the prism, and allowing the subsequent escape through the inclined sides of the dove prism. A moderately focused (spot size ~20 µm) 532 nm wavelength TM-polarized laser beam was directed toward the sample at normal incidence, and the position of the entire assembly was scanned such that the wire crossed the laser beam focus. Optical power detectors were placed both on-axis (angle ~0°) and off axis at an angle close to 60°.
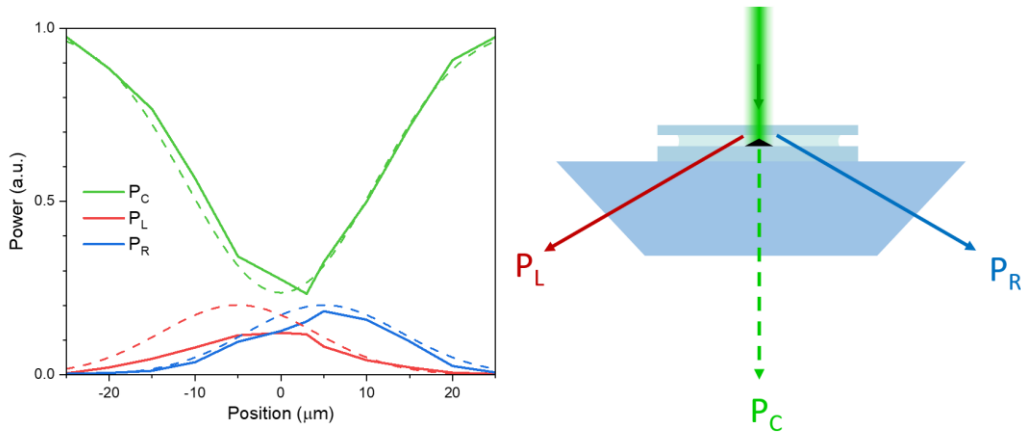
Figure 4.3: Measured transmitted and recovered power obtained from a single light-trapping electrode line as a function of position under focused illumination, as well as the predicted transmitted and recovered powers (dashed line). The measurement schematic shows the location of the three power detectors.

Figure 4.3 shows the position-dependent collected power for the on-axis detector and the two off-axis detectors, as well as a measurement schematic. As the laser spot is moving across the electrode the on-axis transmitted power (green line) gradually decreases, reaching a minimum transmitted power fraction of 24%, and then gradually recovers. As the on-axis transmission reduces, the off-axis collected power on the left side (red line) and right side (blue line) both rise, clearly indicating that part of the reduction in on-axis transmission is accompanied by the trapping and subsequent recovery of reflected light. The full width at half maximum (FWHM) of all three curves is close to 20 μm, similar to the width of the electrode and the laser spot. The maximum collected power for the off-axis detectors occurs at slightly different sample positions, which is due to the fact that the off-axis detectors receive signal from the left and right wire segments

respectively, with center positions that are separated by 10 µm. The two off-axis detectors report slightly different maximum signal strengths, which might be due to a difference in surface quality of the electrode sides. Similar measurements on a flat reference electrode (not shown) did not reveal any detectable power on the off-axis detectors. Theoretical predictions of both on-axis (dashed green line) and off-axis collected signal in the left and right detectors (dashed red and blue lines respectively) are included. The calculations assume an incident Gaussian beam with a FWHM of 20 µm. Any light incident on the 20 µm wide electrode is assumed to be removed from the center detector signal. Of the light incident on the individual 10 µm wide sides of the electrode, 54.9% is assumed to be absorbed by the Cu surface based on literature values [79] for the Cu dielectric function taking into account the incident angle and the incident polarization. The remaining light is assumed to be trapped and collected with 100% efficiency. Note that the calculated curves closely match the width and position of the experimental curves, while the experimental curves for the off-axis detectors are lower than the calculated curves. This difference between the experimental and theoretical collected signal fractions is attributed to a combination of surface imperfections contributing to scattering losses and diffraction, resulting in non-ideal collection by the off-axis optical power meters.

Based on the position dependent power curves in Figure 4.3, the light trapping efficiency η_{LT} was estimated, defined here as the fraction of off-axis collected power relative to the on-axis shadowing losses. Based on both the measurements (solid lines) and the calculated results (dashed lines), an average light trapping efficiency of ~26.5% is found, i.e. 26.5% of light that would normally be lost to reflection is recovered through total internal reflection. Taking into account the

previously mentioned Cu reflection losses, it is estimated that on average 59% of light initially reflected by the electrodes is recovered. As stated previously this value may underestimate the actual trapping efficiency as it does not take into account signal losses due to diffractive effects. This efficiency can be further improved by replacing Cu with more reflective metal such as silver [79], which has low reflection loss (~2.7%) on the surface at TM polarization, leading to potential high light trapping efficiency of 57.23%.

4.6 Summary

In summary, we have experimentally demonstrated a novel light-trapping transparent electrode design. Embedded metallized wires with inclined surfaces were used to direct incident light to reflected angles larger than the critical angle of the embedding medium, resulting in total internal reflection, which in turn allows for recovery of the reflected light. Prototype samples were fabricated using multi-photon lithography and selective chemical deposition. The light trapping process was demonstrated experimentally using optical microscopy and spatially resolved transmission measurements. The measurements indicate that at least 59% of light reflected by Cu electrodes with a surface tilt of 30° is recovered through total internal reflection. The demonstrated design and related structures could significantly improve the efficiency of a wide range of optoelectronic devices.

CHAPTER 5: EFFICIENT GRATING-BASED LIGHT TRAPPING ELECTRODES USING SELECTIVE ZERO ORDER SUPPRESSION

5.1 Introduction

As discussed in Chapters 2-4, light trapping electrodes with inclined surfaces can drastically reduce shadowing losses in optoelectronic devices. While the high performance of such structures is attractive, the fabrication of structures with non-coplanar surfaces poses significant fabrication challenges. It is therefore of interest to investigate alternate approaches that enable large-angle light direction and light trapping in structures that can be defined using standard lithographic methods.

Here we explore the possibility of achieving efficient light trapping based on binary dielectric diffraction gratings defined on metallic wires, as shown in Figure 5.1. Light incident on the metallic wire is diffracted to different angles by the binary grating. The wire and the grating are embedded in a cover layer with a refractive index substantially higher than that or air. With a proper choice of grating spacing, the first order diffracted light appears at an angle beyond the critical angle of the cover layer, leading to light trapping through TIR. This could produce high light trapping efficiency, provided that specular reflection, i.e. diffraction into the zeroth order, is small. In this study, we demonstrate that near-complete light trapping can be achieved with the proper choice of grating spacing, thickness, and duty cycle. The findings are explained in terms of a model that considers destructive interference between fields reflected from the top of the grating and fields reflected by the grating-electrode interface. Based on the obtained optimized structural parameters, light trapping diffractive electrodes were fabricated by e-beam lithography and dry

etching, and their performance was analyzed. Efficient light trapping (>30%) is observed for unpolarized light across a 36° angular range and a 200 nm spectral range at visible wavelengths. The spectral and angular responses of the electrode are experimentally investigated. A maximum light trapping efficiency of 41.4% and near perfect zero order suppression have been experimentally demonstrated for unpolarized illumination, which can be further improved by using low loss dielectric materials. The coplanar nature and the polarization-independent optical response of the presented light-trapping structure enables integration in real-world photodetectors and solar cells.
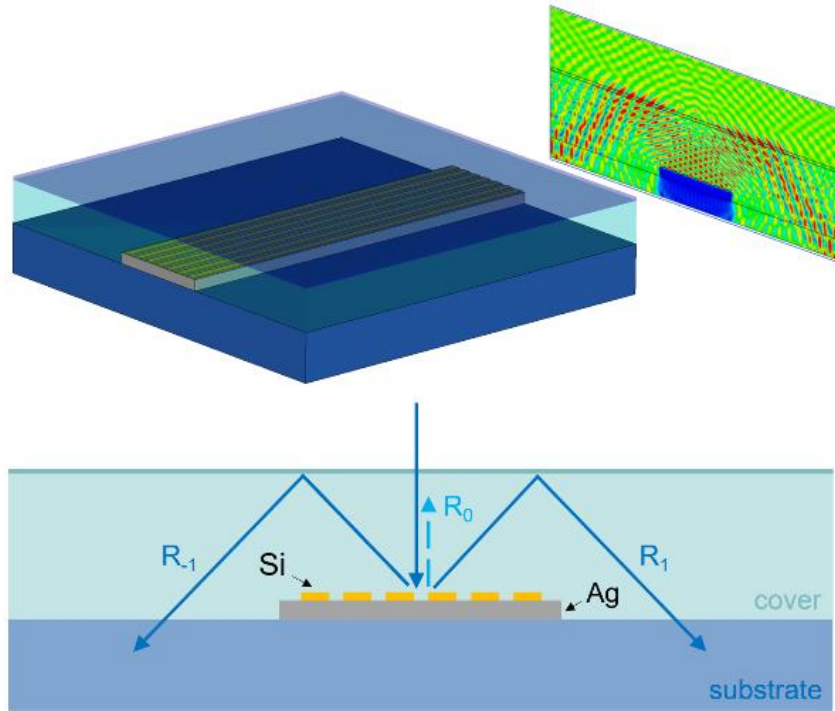
Figure 5.1: Diffractive light trapping electrode design with an example electric field magnitude distribution (top) and a schematic cross section showing the basic principle of operation (bottom).

5.2 Grating design

To assess the feasibility of diffractive light-trapping electrodes we first consider an infinitely extended binary silicon grating on a silver substrate embedded in a homogeneous silica background. Three structural parameters are considered: the grating period L, the lateral Si fill fraction f corresponding to the duty cycle of the grating, and the grating thickness D. The period L is chosen to be sufficiently large to enable first order diffraction, and sufficiently small to ensure that the first diffracted order appears above the critical angle. To satisfy these requirements, the

grating period should lie between the internal and external wavelength, corresponding to the condition $\lambda_0/n<L<\lambda_0$. We initially select a wavelength of $\lambda_0=600$ nm and a grating spacing of L=550 nm.
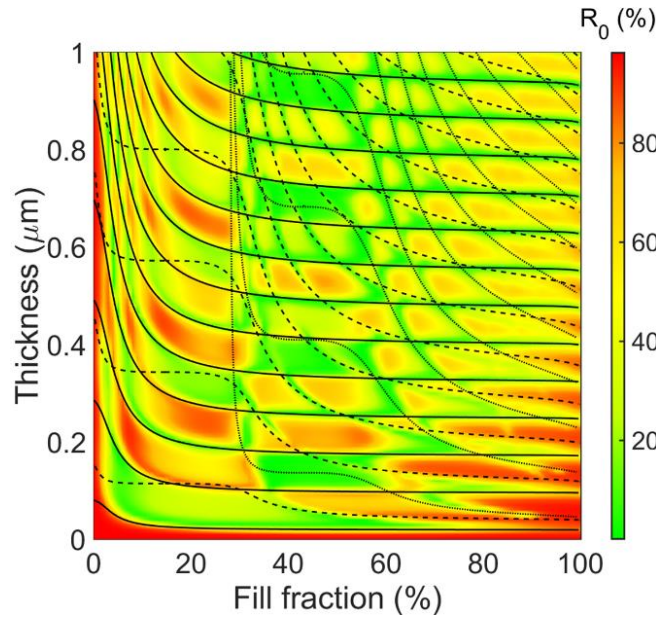
Figure 5.2: Normal-incidence zero-order reflection as a function of Si fill fraction and grating thickness as determined by RCWA. Lines represent predicted locations or reflection minima based on a modal analysis, with minima related to the first three excited grating modes shown as solid, dashed and dotted lines.

The effect of the fill fraction f and the grating thickness D on the normal incidence reflection were studied using rigorous coupled wave analysis (RCWA) [61] with the dielectric functions for Si, Ag, and SiO_2 taken from literature [65, 66, 79]. Figure 5.2 shows the calculated power fraction reflected into the 0th diffraction order (R_0) under TE illumination at $\lambda_0=600$ nm. A complex pattern of reflection maxima and minima is observed. To understand these features, a

model was developed that considers the pathways through which light can contribute to the zero order reflection. The structure is divided into three regions: a homogeneous SiO_2 region representing the cover layer, the patterned Si/SiO_2 grating region, and the metal substrate, see Figure 5.3(c). The incident wave is partly reflected into the zero order at the top of the grating region, corresponding to the primary path for generating a reflected wave, partly diffracted into the SiO_2 region (gray arrows), and partly transmitted into the grating region. The light entering the grating is diffracted into several distinct grating modes that match the periodicity of the grating, schematically indicated by numbered downward arrows in Figure 5.3(c). Under normal incidence illumination, symmetry prevents the excitation of anti-symmetric grating modes. Any excited modes are reflected at the grating-metal interface and partially transmitted back into the zero order (blue upward arrows) constituting a secondary contribution to the zero order reflection, or into the first diffracted order (gray upward arrows), potentially leading to light trapping when using a finite thickness SiO_2 cover layer. The secondary contributions experience a round-trip propagation phase delay of $2Dk_{zi}$ for grating mode i with surface-normal wavevector k_{zi}. We expect reduced reflection when the primary reflected wave destructively interferes with the secondary reflected wave, which occurs for the condition $D=(p+\frac{1}{2})\pi k_{zi}^{-1}$ where p is an integer, assuming a π phase shift upon reflection at the top and bottom of the grating.

Figure 5.3(a) shows the three TE modes that match the periodicity of the grating for f=10%, obtained using the method described in Ref. [80]. The light gray shading indicates the location of the Si region. The lowest order mode (E_0, symmetric) resembles a waveguide mode in the Si region resulting a relatively large propagation constant. The predicted location of reflection minima of

this type of mode is indicated by the solid lines in Figure 5.2. Note that these curves followed the simulated reflection minima closely. The second mode (E_1, symmetric) has a lower propagation constant, requiring larger values of D to generate reflection minima using this type of mode, see the dashed lines in Figure 5.2. The third mode (E_2) is anti-symmetric and thus cannot be excited at normal incidence. At higher Si fill fractions, more modes appear. Figure 3(b) shows five allowed TE modes for f=50% that match the grating periodicity, including one additional symmetric mode (E_4). The predicted locations of reflection minima from this type of mode are shown as the dotted lines in Figure 5.2.

The good correspondence between the locations of the reflection minima calculated using RCWA (green regions) and the model predictions indicate that the observed zero order suppression can indeed be understood in terms of destructive interference by two reflection contributions, one with a mode-dependent phase delay. Note that the lowest order mode (black solid lines) produces a reflection minimum for a small grating thickness D that is only very weakly dependent on the Si fill fraction. This is attributed to the fact that even at a small fill fraction of f=10% the lowest order mode remains predominantly confined in the Si region, resulting in consistently high propagation constant. As a result, a Si-based diffractive light-trapping electrodes are expected to be tolerant to patterning imperfections.
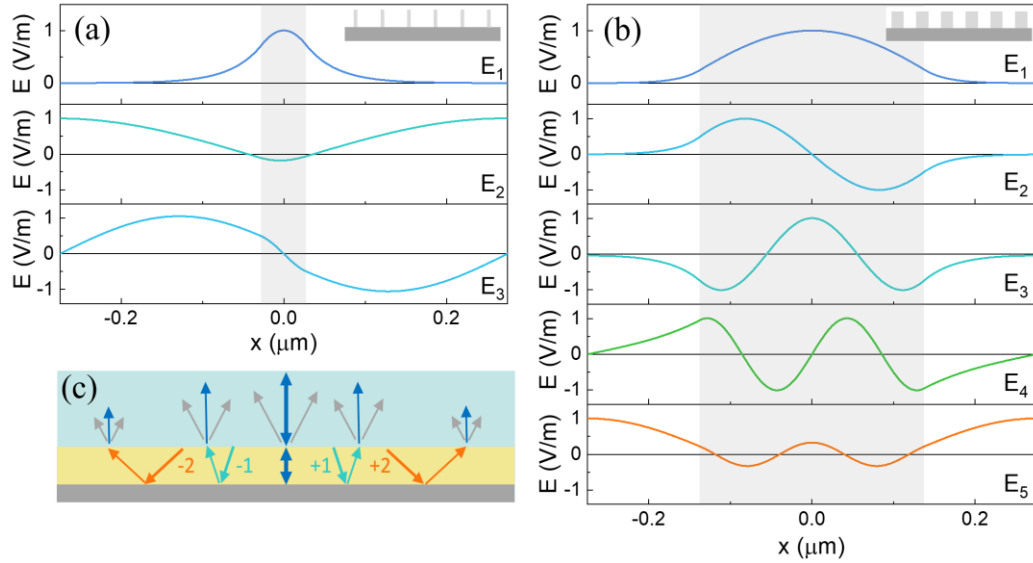
Figure 5.3: (a) Grating modes for *f*=10% and (b) for *f*=50% matching the grating periodicity, shown over a single grating period. (c) Schematic representation of possible light paths, with blue arrows representing the zero order mode.

Next, we use the results from Figure 5.2 to design a diffractive light-trapping interdigitated electrode with suppressed zero order reflection. We focus on a structure with L=0.55 μm, *D*=30 nm, and *f*=54% corresponding to a smallest Si feature size of 0.3 μm. According to the RCWA calculations this design allows for a polarization-averaged zero order reflection as low as 1.1% and an absorption of 6.3%, indicating that potentially 92.6% of the light incident on the patterned metal area could be trapped. The periodically placed metal electrode lines have a width of W=3.85 μm corresponding to seven grating periods as shown in Figure 5.1(a). The metal area coverage is 25%, corresponding to an electrode gap of 11.55 μm. An anti-reflective coating (ARC) optimized for λ_0=600 nm is placed on the silica cover layer, and the distance between the grating

and the ARC layer is 2.28 μm. The metal thickness was set to 400 nm, resulting in an effective

sheet resistance of 0.16 Ω/sq.

5.3 Grating performance

The response of the diffractive trapping electrode design was evaluated using finite element

based simulation. Figure 5.4(a) shows the time-averaged TE field magnitude under normal

incidence plane wave illumination at λ_0=600 nm. The calculated transmission into the substrate

for this geometry is 95.6% despite an only 75% open area, demonstrating efficient light trapping

and strong suppression of the zero order reflection. The field pattern in Figure 5.4(a) clearly shows

the presence of the +1 and the -1 diffracted orders at an angle of 48.4° relative to the normal (solid

arrows), while the zero order diffraction is too weak to produce substantial surface-parallel

standing waves.
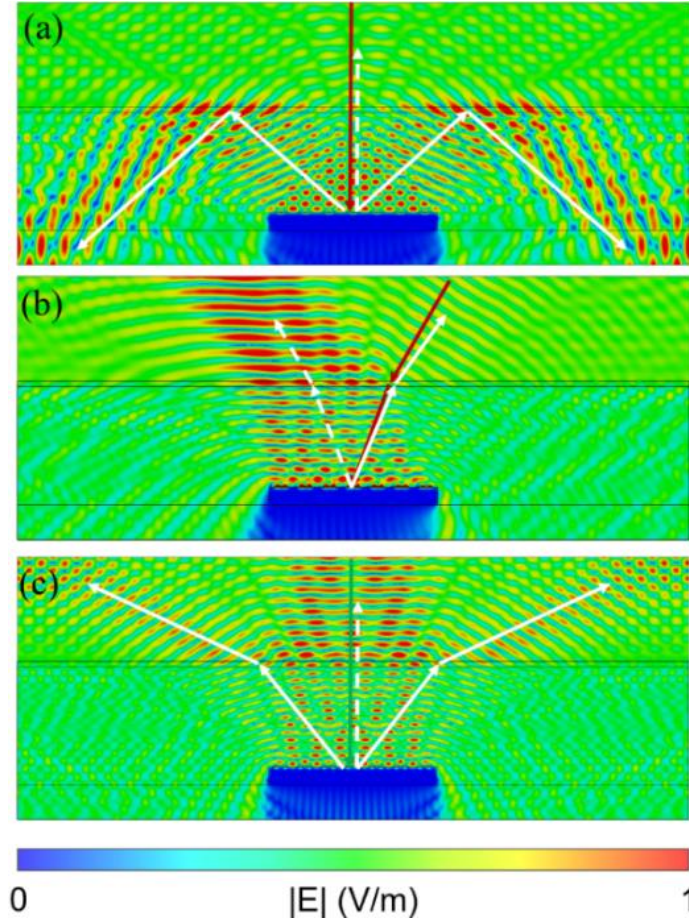
Figure 5.4: Average TE field magnitude for a diffractive light trapping electrode excited at (a) λ_0=600 nm and θ_{inc}=0°, (b) λ_0=600 nm and θ_{inc}=30°, (c) λ_0=500 nm and θ_{inc}=0°.

Figure 5.5(a) shows the angle dependent transmission of the structure in Figure 5.4(a) for TE and TM illumination as well as for unpolarized light (T_{ave}). For reference the response without the grating (dotted line) and without the metal or grating (dashed line) are included. The latter curve, which we call $T_{max}(\theta)$ represents the transmission under perfect light trapping. Figure 5.5(a) also includes the light-trapping efficiency η_{LT} defined as $\eta_{LT}=(T-T_{min})/(T_{max}-T_{min})$ where $T_{min}=(1-f)T_{max}$ represents the ray-optics prediction of the transmission in the absence of the grating.

63

Defined this way, η_{LT} is equivalent to the reduction in shadowing losses, with $\eta_{LT}=1$ corresponding to complete elimination of shadowing effects.

A light trapping efficiency of 82.3% is achieved at normal incidence, representing a more than five-fold reduction in shadowing. Note that this result is quite close to the best-case prediction of 92.6% based on RCWA calculations for an infinitely extended grating. As the angle of incidence increases, the light trapping efficiency drops, reaching values below 30% at angles beyond ~18°. The observed trends can be understood in part by considering the generated internal diffracted angles. Figure 5.5(c) shows the analytically calculated internal angles (i.e. inside the cover layer) of the -1, 0, and +1 diffracted orders as a function of the external angle of incidence. At normal incidence, nearly all reflected power is redirected into the +1 and -1 diffracted orders, both of which appear at angles above the critical angle (horizontal dashed lines) leading to efficient light trapping. At $\theta_{inc} > 6°$ the angle of the -1 order drops below the critical angle, causing a loss of TIR and accounting for part of the drop in light trapping efficiency. At $\theta_{inc}=21.5°$ the +1 order ceases to exist, closing one of the channels for light trapping. Figure 5.4(b) shows the TE field distribution corresponding to the case of $\theta_{inc}=30°$ with near-zero light trapping efficiency, where the -1 order is absent, and the +1 order (white solid arrow) appears below the critical angle. Meanwhile, the zero order suppression is seen to break down, as evidenced by the strong standing wave in the air region above the metal wire. This is attributed to angle-dependent changes to the reflection phase shifts at the top and bottom of the grating. Despite these effects, a transmission of T>82% is achieved with $\eta_{LT}>30\%$ over a 36° angular range about the surface normal. The transmission is

found to be relatively polarization independent, with similar values for TE (light gray line) and

TM (dark gray line) polarized light.
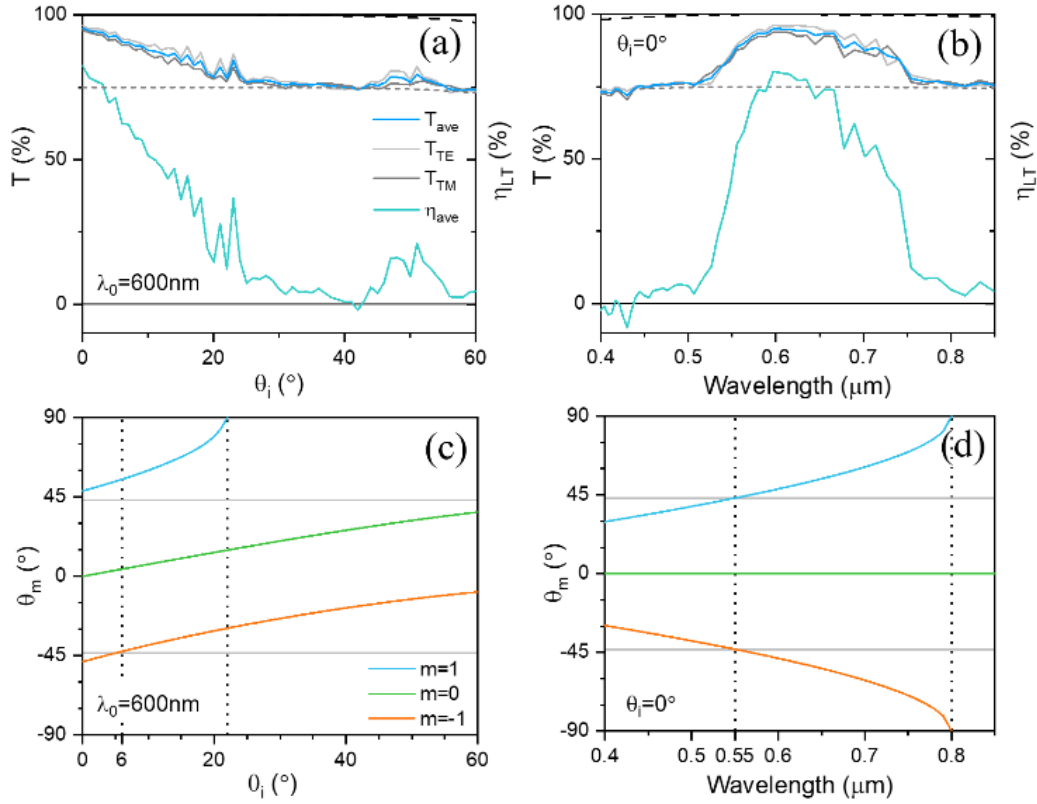
Figure 5.5: The (a) angular and (b) wavelength dependent transmission of a diffractive light-trapping electrode with a metal area coverage of 25%, and (c) the diffraction angle of order _m_ as a function of angle of incidence and (d) wavelength.

Next, we investigate the spectral response of the diffractive light trapping electrode. Figure

5.5(b) shows the same quantities as in Figure 5.5(a) as a function of incident wavelength under

normal incidence illumination. Maximum transmission occurs at 600 nm corresponding to the

previously observed polarization-averaged transmission of T=95.6% with a light trapping

efficiency of η_{LT}=82.3%. A light trapping efficiency in excess of 30% is observed in the wavelength range 540 nm - 740 nm, with a spectrally-averaged transmission of T=91% and an average light-trapping efficiency of η_{LT}=62 % for unpolarized light. A relatively rapid drop in the light trapping efficiency is observed for short and long wavelengths, predominantly due to the wavelength-dependent diffraction angles as illustrated in Figure 5.5(d). At wavelengths larger than 750 nm, the diffracted light appears at sufficiently large angles to reach the neighboring electrode line. This results in some of the diffracted light being redirected out of the structure, an effect that we have previously called secondary shadowing [59]. At λ_0>800 nm, no diffracted orders can be generated in the cover layer, preventing any diffraction-mediated light trapping. At wavelengths shorter than 550 nm, the diffracted angles fall below the critical angle, resulting in a loss of TIR and a low light trapping efficiency. An example of such a scenario is shown in Figure 5.4(c) for an incident wavelength of λ_0=500 nm. The first order diffracted light is clearly visible in the region above the silica layer, illustrating the breakdown of light trapping for short illuminations wavelengths.

5.4 Experimental demonstration

To experimentally demonstrate the aforementioned performance of the light trapping electrode, a proof-of-concept sample were fabricated using e-beam lithography, Si deposition and dry etching. Here we used Au instead of Ag for the sake of fabrication feasibility, which does not significantly affect the ability of light trapping of the electrodes since Au also has high reflectivity in the visible range. The detailed fabrication workflow is shown in Figure 5.6. In brief, the negative

lithography was done by using MJB3 mask aligner and NR7-1000PY negative photoresist to open windows for 480 μm gold strip deposition. Then 5nm of Titanium and 300nm of gold were deposited using Edwards's thermal evaporation machine. Then 32 nm of Si was deposited on top of the gold layer. The Si deposition was done by using temescal FC-2000 E-beam evaporator at 4×10^{-7} torr.

The zero order suppression grating was fabricated on the gold strip using the following procedures: 300 nm of E-beam lithography (EBL) mask layer was created on top of Si layer by spinning coating 495 A6 PMMA solution at 3500 rpm for 60 s and pre-baked at 180 °C for 1 min. Then EBL was conducted at 10 nA current and 200 μC/cm^2 dose using Leica 5000+ e-beam lithography instrument. The exposed area was washed away in IPA: deionized water 7:3 solution for 2min to develop the nanostructure. Then CF4:SF6 (50:70) reactive ion etching (RIE) was used to transfer the grating patterns to the Si layer. The sample was immersed in acetone for 12 hours to lift-off the sample and remove the PMMA.
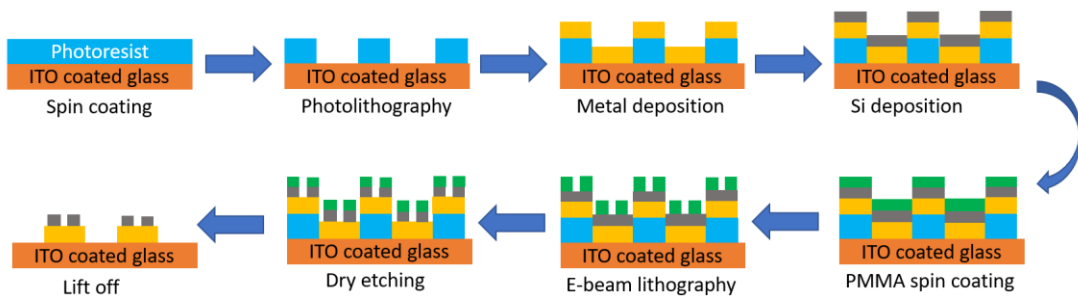
Figure 5.6: Process flow of the fabrication of grating-based light-trapping electrodes.
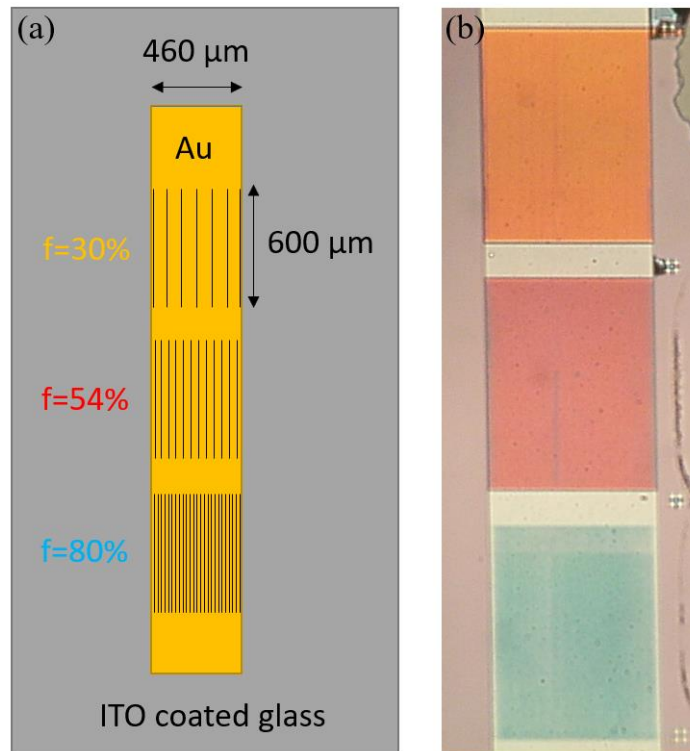
Figure 5.7: (a) Schematic sample layout showing three light-trapping grating regions with silicon fill fractions f=30%, 54% and 80%. (b) Bright-field reflection microscopy images of the grating based light trapping structures.

Figure 5.7(a) shows the sketch of the sample. A 480 µm wide Au metal stripe is deposited on top of the ITO coated glass. Shallow Si gratings with different fill fractions are deposited on top of the metal stripe. Among them the gratings with f=54% are our target sample while those with f=30% and 80% are the references. All gratings share the same length of 600 µm and width of 480 µm, covering the entire metal stripe.

Reflection microscopy images of the fabricated structures without cover layer are shown in Figure 5.7(b). Gratings with f=30%, 54% and 80% are shown from top to bottom, following the

sequence in Figure 5.7(a). The objective lens has 5× magnification and a numerical aperture of NA=0.15, corresponding to a small maximum collection angle of 8.63°. At this magnification the individual grating lines cannot be resolved. The different gratings are seen to produce distinct color difference, with the f=30% region exhibiting a predominantly orange color, the f=54% region a red color, and the f=80% region a blue-green color. This may seem surprising since the grating period is identical for all three regions, and therefore one would expect the same colors to be diffracted outside the numerical aperture of the objective. The distinct colors of the different regions is therefore attributed to a different diffraction efficiency. Note that these structures were designed to be used as embedded gratings, and therefore the optimum performance requires the presence of a cover layer.

In order to evaluate the zero-order suppression and light trapping efficiency for the fabricated structures, the sample was covered by a 200 µm thick glass cover slip and a drop of index-matching liquid (n=1.518) was placed between the sample and the cover slip. The cover glass and index matching oil together form a near-uniform dielectric cover layer. The covered sample was imaged in bright-field reflection microscopy. A sketch of the measurement setup is shown in Figure 5.8(a). A small aperture stop was used in the illumination path to provide near-normal incidence. First-order diffracted light appears at angles beyond the critical angle, resulting in light trapping. For efficient light trapping, we thus expect that the grating region looks dark, and for broadband light trapping it is expected that the grating region does not have a pronounced color. Figure 5.8(b) shows the region with a Si fill fraction of f=30%, taken near the left edge of the grating region using a 50× objective (N.A.=0.8). Note that the grating-covered gold wire has a

similar brightness as the cover slip region (left side of image), suggesting relatively low reflection from the metallic region. The grating region has a reddish hue, suggesting short wavelength light is either trapped or absorbed by the grating region. Figure 5.8(c) shows the region with a Si fill fraction of 54%. Note that the metallic region appears darker than the surrounding glass region, indicating stronger zero-order suppression and potentially larger light trapping efficiency than the f=30% region. Finally Figure 5.8(d) shows the region with a Si fill fraction of 80%. Note that this region appears significantly brighter than the grating regions in Figure 5.8(b) and (c), indicating a significantly reduced zero-order suppression. The results in Figure 5.8 confirm that the Si fill fraction is an important parameter in achieving minimum specular reflection, which in turn enables large light trapping efficiency.
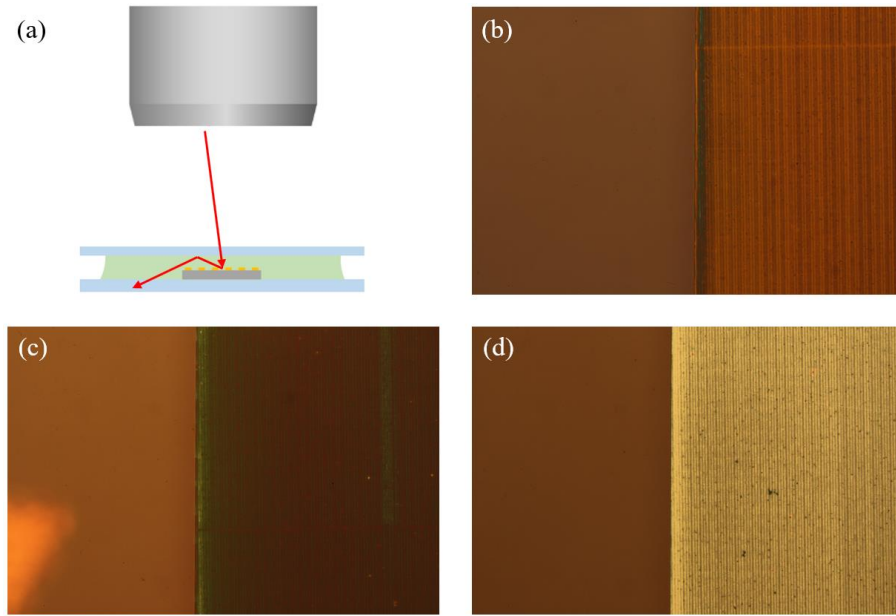
Figure 5.8: (a) Schematic of the glass-covered light trapping electrodes and the reflection microscopy images of the gratings with (b) f=30% (brown), (c) f=54% (dark green) and (d) f=80% (white).

While the microscopy images strongly suggest that the optimized grating-based light-trapping structure enables strong shadowing reduction, quantitative measurements are needed. To assess the spectral dependence of the light trapping efficiency, we measured the reflection spectrum (R) of the electrodes at different polarizations using a microscope-coupled spectrometer. A small aperture stop was used to ensure near-normal illumination. We used an objective lens with 5× magnification (N.A.=0.15). The measured reflection spectra are shown in Figure 5.9(a). The spectra were intensity normalized using a clean single-crystal Si wafer as a reference. The reflectance of TE and TM polarized light are shown in blue and red lines respectively. Low reflectance (<8%) is observed from 500 nm - 700 nm for both polarizations. At longer wavelengths

(700-800 nm), R_0 increases to ~15% at λ=800 nm for TE polarization and to ~26.5% for TM polarization. While this measurement cannot distinguish light trapping from absorption in the a-Si grating regions, it does suggest that the zero-order suppression is effective across a wide spectral range, similar to the predictions made in Figure 5.5(b).

Next we investigate the zero order suppression efficiency, which we define as η_{zs}=1-($R_{grating}$-R_{glass})/(R_{metal}-R_{glass}), in which $R_{grating}$, R_{metal} and R_{glass} are the measured reflectance values measured when the light is incident on the grating, a glass covered bare Au stripe, and an isolated glass cover slip. The value of R_{glass} was divided by two to remove the backside reflection contribution. This definition removes the constant top-surface reflection loss, which intrinsically cannot be suppressed by the grating structure. In real devices, the cover layer itself would be coated with an anti-reflective coating to further improve the overall transmission. The thus obtained zero order suppression efficiencies for different polarizations are shown in Figure 5.9(b), using by the same colors as in Figure 5.9(a). Note that the y-axis (η_{zs}) is shown in the range 75% - 100%. For TE polarization, a strong zero order suppression of η_{zs}≈92.9% is observed at λ=500 nm, followed by a gradual increase at longer wavelengths. A near perfect zero order suppression range is observed from 600 nm – 740 nm, following the simulation results in Figure 5.5(b). For TM polarized illumination, near 100% zero-order suppression is observed from 500 nm – 650 nm, followed by a gradual decrease to 76% at 800 nm.
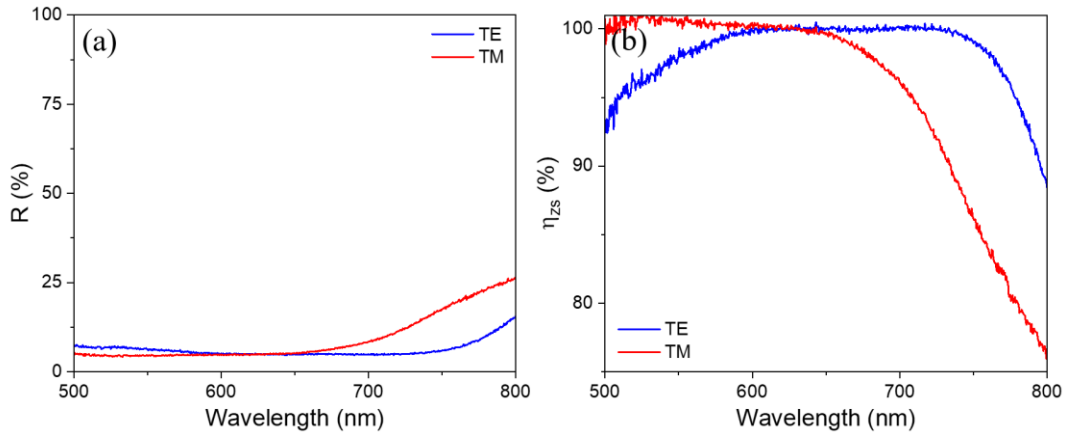
Figure 5.9: (a) The reflection spectra of a Si-grating covered Au light trapping electrode under TE and TM polarized illumination, and (b) the corresponding zero-order suppression efficiency spectra.

The large observed zero-order suppression efficiencies observed in Figure 5.9 are expected to be due to a combination of light trapping and absorption by the a-Si grating regions. To distinguish the relative contributions of these two factors, in the following we directly measure the fraction of trapped light under normal incidence illumination of the light trapping electrode with f=54%. The optical setup we used to measure the light trapping efficiency is shown in Figure 5.10(a). The glass-covered light trapping electrodes are placed on top of a dove prism to allow measurement of off-axis recovered (trapped) light. Index matching oil is added between the sample and the Dove prism to allow transmission of trapped light into the prism, A He-Ne laser with 633 nm wavelength was used as the light source. The laser spot size had a FWHM of ~300 µm. The position of the entire assembly was scanned such that the wire crossed the laser beam. Identical optical power meters were placed both on-axis and off-axis at an angle close to 50°. Based on the collected power the light trapping efficiency was determined, defined as $\eta_{LT}=(P_R + P_L)/(P_{T0} - P_{T1})$,

in which P_R is the off-axis power collected on the right side, corresponding to the trapped -1 diffracted order, while P_L is its counterpart on the left side corresponding to the trapped +1 diffracted order. P_{T1} represents the on-axis transmitted power when the laser is incident on the grating region, while P_{T0} represents the on-axis transmitted power when the laser passes through a transparent area near the light trapping electrode. Using this definition the light trapping efficiency represents an estimate of the shadowing reduction, i.e. the recovered power relative to the power blocked by the patterned electrode region.
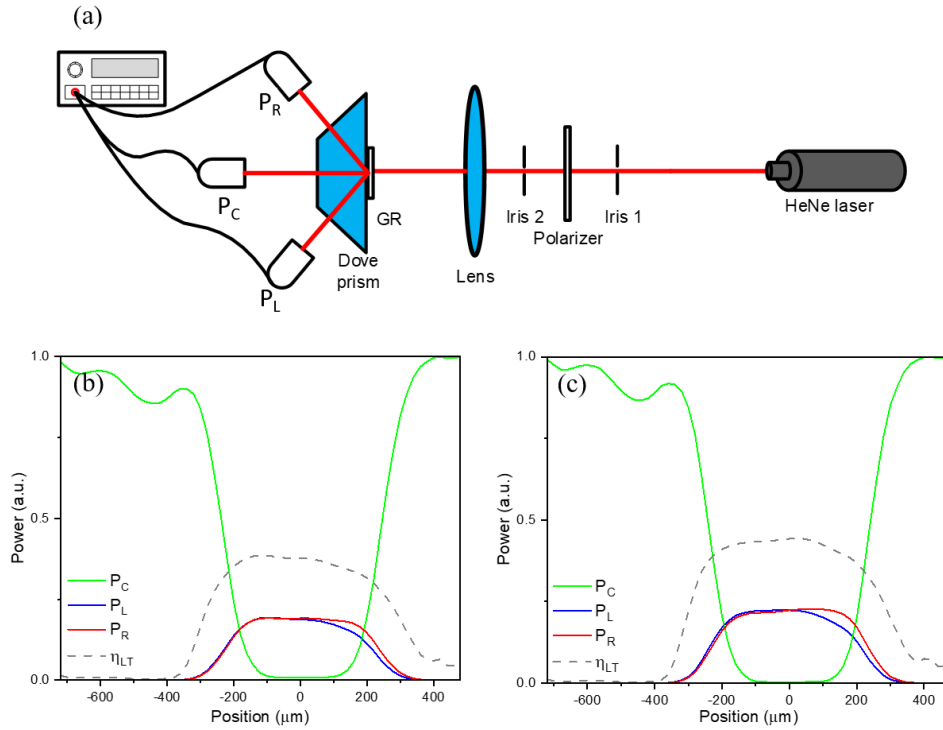
Figure 5.10: (a) Schematic of the optical setup that measures the light trapping efficiency of the sample. Measured on-axis (green line) and off-axis (red and blue) transmissions obtained from the grating-based light trapping electrode as a function of the position in x-axis under focused illumination at (b) TE and (c) TM polarization. The inferred light trapping efficiency are included (grey dashed line).

Figure 5.10(b) and (c) show the measured on-axis transmitted power (P_C) and the off-axis recovered power (P_L: left detector and P_R, right detector) as a function of the position. All measured powers are normalized by the maximum transmitted power when the light is incident on an unmetallized region. In Figure 5.10(b), as the laser spot moves across the ~400 μm wide light trapping electrode, the on-axis signal (green line) reaches near-zero transmission (<1%), indicative of strong shadowing by the grating covered metallic wire. Small fluctuations of P_C are seen

observed at x<-340 μm. This is attributed to signal loss due to the presence of a small air bubble that was observed near the grating edge in prior reflection microscopy measurements (not shown). As the on-axis signal drops, the off-axis recovered power by the left and right detectors (blue and red lines) gradually increases from zero to ~19% when the laser spot is close to the center of the electrode, resulting in a maximum light trapping efficiency (grey dashed line) of ~38%. This means 38% of the light incident on the electrode is recovered by the grating. For TM polarization similar observations are made, showing a slightly higher light-trapping efficiency of ~44.3%. The observed efficiencies represent a lower bound, given the non-zero angular spread of the diffracted beams and the finite size of the power meters. Comparing the observed minimum trapping efficiency of 38% with the observed zero order suppression efficiency of ~100% at 633nm (Figure 5.9(b)), it appears that as much as 62% of the incident light may be absorbed by the light trapping grating. Such large absorption losses may be due to the large absorption of the deposited amorphous silicon gratings. To investigate this possibility, RCWA calculations were carried out taking into account literature values for the dielectric functions of amorphous silicon [81] and gold [79] for a grating fill factor of the f=54%. The calculated absorption loss at λ=633 nm is 55% for TE polarization and 42% for TM polarization. Based on these results it appears that the light trapping itself is quite efficient, with a large fraction of lost power attributed to absorption in the grating region.

5.5 Summary

In summary, a transparent light trapping electrode consisting of a binary embedded dielectric grating placed on metallic wires was theoretically investigated and experimentally demonstrated. Shadowing losses in an example electrode with a 25% metal coverage were numerically shown to be reduced by more than a factor five under normal incidence illumination at 600 nm, and a light trapping efficiency in excess of 30% was obtained over a 36° angular range about the surface normal. The spectral performance was investigated, and the simulated light trapping efficiency was found to exceed 30% for wavelengths in the range 540 nm - 740 nm, with a spectrally-averaged light trapping efficiency of 62 % for unpolarized light. The light trapping process was found to be relatively insensitive to polarization. In experiments on a prototype diffractive light trapping electrode a light trapping efficiency of 41% was observed for unpolarized illumination at normal incidence. The trapping efficiency may be increased by using a lower loss dielectric in the grating region.

CHAPTER 6: SUPPRESSION OF REFLECTION LOSS IN GRADIENT METASURFACE OPTICAL ELEMENTS

6.1 Introduction

Previous chapters discussed reflective light-trapping electrodes that utilized redirection of incident light toward angles beyond the critical angle, resulting in light recovery via total internal reflection. An alternate approach to reducing shadowing loss involves redirecting the incident light to avoid interaction with metallic electrodes entirely, e.g. using indentations in a dielectric cover layer as shown in Figure 6.1(a) or using micro lens arrays above interdigitated electrodes. While such approaches can provide strong shadowing reduction, the involve non-coplanar outer surfaces. An alternate approach that could produce similar light redirection involves the use of gradient metasurfaces. Applying a thin high-index region with gradually varying refractive index, it is possible to achieve functionality similar to that of a Fresnel lens, enabling redirection of light using coplanar structures, as schematically shown in Figure 6.1(b). While metasurface-based light redirection appears to be a promising approach for mitigation of contact shadowing losses, one challenge involves the incurred reflection losses.

Metasurface optical elements that rely on propagation phase typically make use of varying fill fractions of high refractive index materials such as TiO_2 (n~2.4-2.8) or a-Si (n~3.5-5), resulting in regions with significantly different effective refractive index across the surface. This index gradient makes it a non-trivial task to eliminate reflection losses across the entire optical element. Minimizing such surface reflections from metasurface optical elements remains a relatively unexplored area. Here we investigate the optical performance of high-index gradient metasurfaces.

We demonstrate that a drastic reduction of surface reflections is possible through the application of an anti-reflective layer with a thickness and refractive index that are substantially different from the traditional bulk optics values. It has been demonstrated that the optimized anti-reflective coating outperforms the standard approach by a factor of 5 for metasurfaces with <73% areal fill fraction.
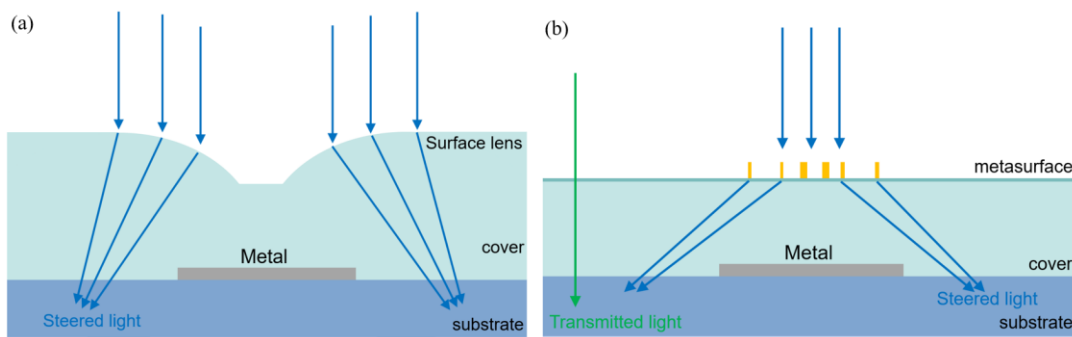
Figure 6.1: Schematics of (a) surface micro lens array and (b) metalens array. Both elements are used to redirect the incident light into the substrate to reduce the reflection losses.

The advent of metasurface optics has led to a wide range of applications of flat optical devices, including active wavefront control [51, 82, 83], sensing [44-46], imaging [84-86] and 3D display [48, 49]. Metasurface optical elements have been found to approach or exceed the performance of traditional optical elements in certain scenarios. They offer unprecedented flexibility in optical functionality using compact structures that can be fabricated through standard 2D lithographic techniques. Despite the many appealing aspects of metasurface optical elements, their unique design introduces new challenges in optical systems. One interesting challenge is the issue of reflection losses from metalenses and related structures. In imaging systems, even a small amount of reflection from optical elements can lead to notable image artifacts in high-contrast

images. In traditional optics these issues are mitigated by the application of anti-reflective coatings (ARC) using well-known design rules. However, as we will show here, for gradient metasurfaces based on propagation phase the traditional design rules are not practical, causing significant spatially varying reflection losses.
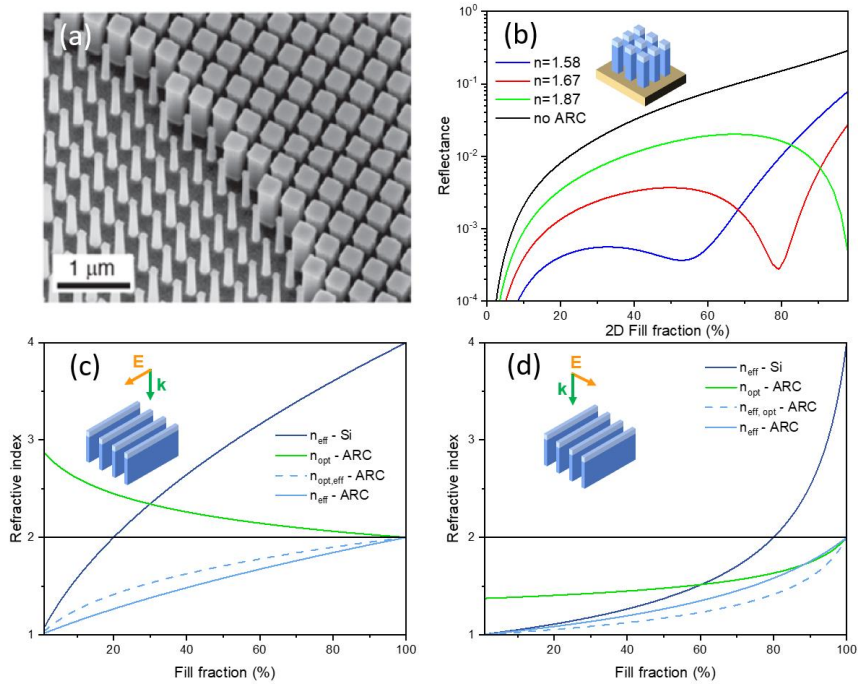
Figure 6.2: (a) SEM image of a Si-based metasurface lens, taken from Ref. 83 [87]. (b) Calculated reflectance values for Si metasurfaces without ARC (black line), with n_{ARC}=1.87 (red line), n_{ARC}=1.67 (blue line), and n_{ARC}=1.87 (green line). (c) Predicted effective index of pillars made of a material with n=4 (orange line), the traditional refractive index choice for the ARC coating (black line), the resulting effective index of the ARC region (solid blue line), the desired effective index of the ARC region (dashed blue line), and the desired index of the ARC material to achieve the desired effective index (green line) for (c) TE and (d) TM polarizations respectively.

6.2 Theory

A traditional thin-film ARC eliminates back-reflection from a high-index optical element by introducing two reflecting interfaces, each producing a reflected field of equal amplitude, where one of the reflected fields incurs a phase delay of π radians. For the correct choice of ARC index and thickness, the reflected fields destructively interfere, resulting in zero reflection and perfect transmission. For a bulk optic with known index n_{sub} surrounded by air, the traditional ARC index n_{ARC} and thickness d_{ARC} are given by $n_{ARC}=\sqrt{n_{sub}}$ and $d_{ARC}=\lambda_0/4n_{ARC}$ respectively. However, as we demonstrate in the following, this traditional choice of ARC design cannot easily be transferred to metasurface optical elements. Gradient metasurface optical elements typically make use of lateral patterning of a high-refractive index layer to achieve effective index gradients, allowing spatially varying propagation phase delays. As an example, Figure 6.2(a) shows a region of an amorphous silicon-based metasurface lens (image from Ref. [83]) revealing strong local variation of the silicon fill fraction across the lens surface. It is the resulting spatial variation of the effective index that poses a challenge: in order to achieve the lowest possible reflection, each region of the metasurface would require a specific ARC thickness and index, neither of which can be easily ensured using standard fabrication steps. In this study we first demonstrate this challenge in detail, followed by a proposed mitigation strategy that produces significantly reduced reflection losses across a wide range of fill fractions that is compatible with traditional device processing steps.

To illustrate the challenge and its impact, Figure 6.2(b) shows the reflectance at $\lambda_0=1550$ nm of a silicon-based metasurface for a range of fill fractions, calculated using Rigorous Coupled Wave Analysis (RCWA) [61]. The structure consists of an infinitely extended

82

metasurface containing square silicon pillars (n=3.5) in air, with a width W placed on a regular square lattice with period L=200 nm. The horizontal axis represents the Si areal fill fraction $f=(W/L)^2$. Without any ARC applied (black curve) regions with large fill fraction suffer from a surface reflection loss as high as 30.9%. As the fill fraction is reduced, the effective index drops, which results in a drop of the reflection loss. To further reduce the reflection loss, a seemingly reasonable approach is to apply an ARC on the Si layer before patterning, using the traditional index choice and thickness. After patterning the metasurface, this produces the structure shown in the inset. This results in a large drop in reflection for high fill fractions (green curve), but the reflection rapidly increases as the fill fraction is reduced. This failure of the standard approach is intrinsic to AR-coated gradient metasurfaces but can be significantly mitigated, as will be shown below.

To illustrate the fundamental reason for the breakdown of the standard ARC approach on metasurfaces, we first consider an effective medium description for two different 1D situations. Figure 6.2(c) shows the calculated effective index of a deeply subwavelength grating for a material with index n=4 as a function of fill fraction (orange line) under TE excitation. As the fill fraction of the high-index rods is reduced, the effective index $n_{eff,rods}$ drops gradually. At each fill fraction, the optimum AR coating index would be given by $n_{opt}=\sqrt{n_{eff,rods}}$ as shown by the dashed blue line. However, in practice when the high index layer is coated with a layer that has the traditional $n_{ARC}=\sqrt{n}$ before patterning, after patterning this produces a non-ideal $n_{eff,ARC}$ indicated by the blue solid line. For all fill fractions $0<f<1$ the obtained effective index of the ARC region $n_{eff,ARC}$ is less than the ideal value, based on analytical effective medium theory. To compensate for this effect,

83

the 1D metasurface would have to be coated with a material that has a different index for each separate fill-fraction, with an index that is higher for lower fill fractions (green line). In addition, for each region there would be a unique optimum thickness (not shown) given by $\lambda_0/4n_{eff,opt}$. For TM polarization (Figure 6.2(d)) the fill-fraction dependence is quite different, but as in the TE case, the optimal ARC material index would be different for each fill fraction used. These examples highlight that even in idealized 1D metasurfaces, applying a traditional ARC before patterning *intrinsically* leads to deviations of the ARC index from the optimum value for all fill fractions $0<f<1$.

As demonstrated above, no single ARC material choice produces perfect AR behavior across all metasurface fill fractions. Next, we investigate improved choices for both the refractive index of the ARC material and the thickness of the patterned ARC layer to be applied on an isotropic Si metasurface. We consider a metasurface intended for use at a wavelength of 1550 nm ($n_{Si}=3.5$) with a unit cell size of L=200 nm. Figure 6.3(a) shows a contour graph of the reflectance as a function of Si fill fraction and ARC layer thickness calculated using RCWA, where the ARC index is set to the traditional value of $n_{ARC}=\sqrt{n_{Si}}$. The reflectance is shown on a log scale from 0.01% to 10%, with green regions indicating a reflectance below 0.1%. For low Si fill fractions, the reflectance is always low, independent of the AR layer thickness, since in this region the metasurface has a refractive index close to that of air. For a Si fill fraction of 1, we see that minimum reflection of ~0.01% is achieved close to $d_{ARC}=207$ nm, corresponding to the traditionally expected optimum thickness of $d_{ARC}=\lambda_0/4n_{ARC}$ as indicated by the black dot on the

contour graph. However, for intermediate Si fill fractions the reflectance at this thickness

(d=207nm) exceeds 1% at many fill fractions, as shown in Figure 6.2(b) (red line).
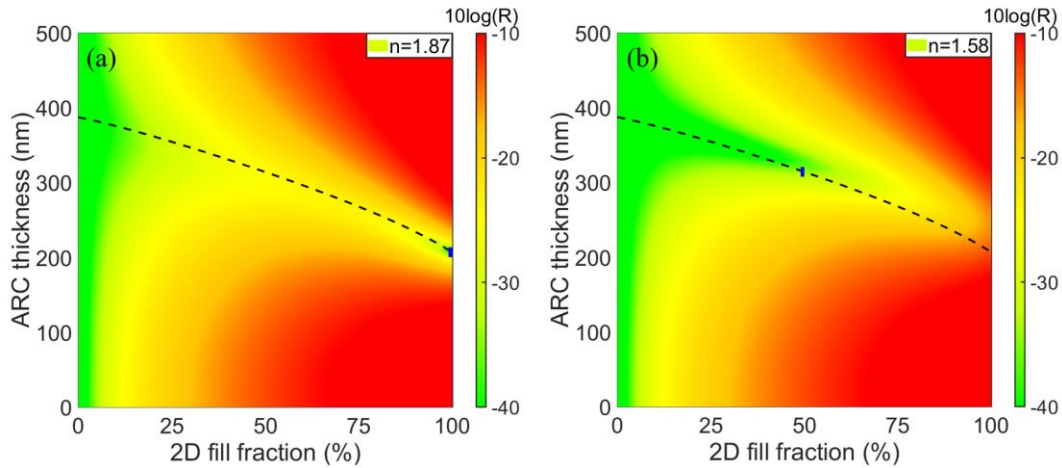
Figure 6.3: Contour graphs of the reflectance at λ_0=1550 nm of a Si metasurface with unit cell size of L=200 nm as a function of Si areal fill fraction and ARC thickness for (a) an ARC refractive index of 1.87 and (b) an ARC refractive index of 1.58.

In order to reduce the reflection for intermediate Si fill fractions (i.e. for values of *f* that are more commonly used in metasurface lenses) we look for modified ARC index and thickness values that provide better performance across a wide fill factor range. As a starting point we use a 2D effective index model [88] to estimate the effective index of a medium consisting of square pillars with dielectric function ε_r in air. This approach predicts an effective relative permittivity given by

$$\varepsilon_{eff} = \left(1 - \sqrt{f}\right) + \frac{\sqrt{f}}{(1-\sqrt{f})+\sqrt{f}/\varepsilon_r} \tag{6-1}$$

This formula is most accurate for high-fill-fraction subwavelength square gratings, but nevertheless provides a useful guideline in choosing an appropriate ARC material index and layer

85

thickness. Based on the effective medium model we can estimate the effective index of the patterned Si region $n_{eff,Si}$ for any fill fraction. We then use the same effective medium model to find the ARC *material* index needed to achieve the corresponding optimum $n_{eff,ARC}=\sqrt{n_{eff,Si}}$. Finally, we determine the optimized ARC thickness given by $d_{ARC}=\lambda_0/4n_{eff,ARC}$. The black dashed line in Figure 6.3(a) shows the resulting predicted optimum ARC layer thickness for each *f* based on the effective medium model approach.

We achieve reduced reflection across a wide range of fill fractions by optimizing our ARC material and thickness for a Si fill fraction of *f*=0.5. At this fill fraction the effective medium model predicts $n_{Si,eff}$ =1.53, which requires an $n_{eff,ARC}$ of 1.24 for minimum reflection. To achieve this effective ARC index, the effective medium model predicts that we require a material with n_{ARC}=1.58, with a corresponding optimum d_{ARC}=314 nm. Figure 6.3(b) shows the reflectance contour graph obtained using RCWA for this optimized fixed ARC material index. The optimized thickness is indicated by the black dot. Note that low reflection is indeed achieved near the calculated thickness at a fill fraction of *f*=0.5, showing good correspondence with the effective medium-based prediction. The resulting reflectance as a function of fill fraction for this *fixed* choice of n_{ARC} and d_{ARC} is included in Figure 6.2(b) (green line) as well as the corresponding curve optimized for *f* =0.75 (blue line). Note that in the latter case, R<0.5% can be achieved for a wide range of fill fractions spanning from 0% to 88%, whereas the traditional ARC parameter choices would lead to significantly larger reflectance across this same region. This range of fill fractions includes the most common fill fractions used in gradient metasurfaces, since fill fractions close to zero and close to one are typically avoided due to the need for impractically small features sizes.
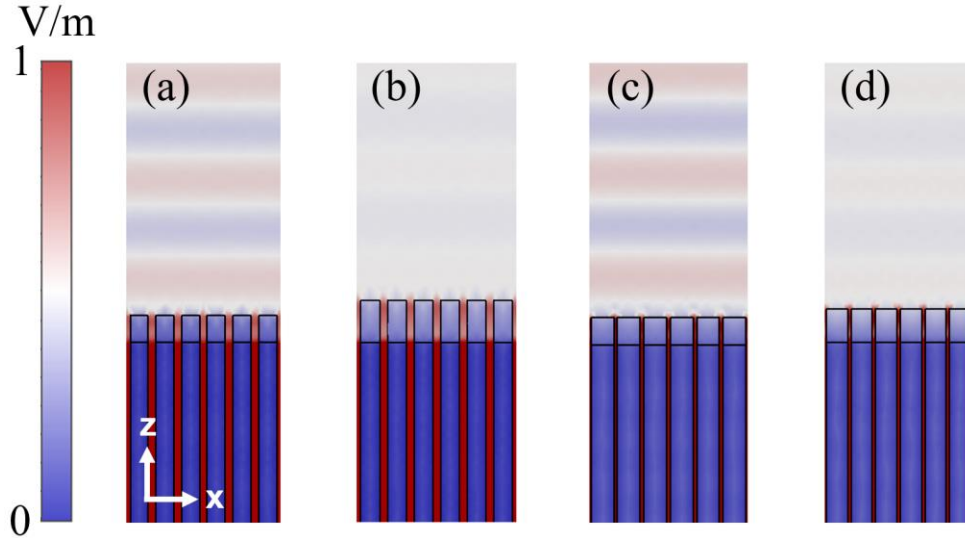
Figure 6.4: Average electric field magnitude above four metasurfaces containing square Si pillars placed on a 200 nm square lattice under illumination at λ_0=1550 nm, with the electric field polarized in the plane of the figure. (a) f =50%, traditional ARC approach (b) f =50%, ARC optimized for f =50%, (c) f =75%, traditional ARC approach and (d) f =75%, ARC optimized for f =75%.

To demonstrate the difference between the traditional approach (i.e. applying a standard AR coating followed by patterning) and the optimized approach, Figure 6.4(a)-(d) show a cross-sectional view of the time-averaged E-field magnitude above 2D Si-based metasurfaces when illuminated with λ_0=1550 nm for a meta-atom size of L=200 nm. The 2D cut is through the center of the Si pillars, and the electric field is polarized along the x-direction. Figure 6.4(a) and (b) show the traditional and optimized ARC for a Si fill fraction of f=0.5. Note the significant larger layer thickness required to achieve optimum performance at f=0.5. The standard approach is seen to

produce a significant standing wave pattern above the surface, which is almost entirely eliminated when using the optimized approach. Figure 6.4(c) and (d) show the equivalent graphs for f=0.75. The thickness difference between the two approaches is not as distinct in this case, however again, a substantial standing wave pattern is observed when using the traditional ARC approach (Figure 6.4(c)), which is again almost entirely eliminated when using the optimized ARC structure (Figure 6.4(d)).

6.4 Summary

In summary, we have studied the suppression of first-surface reflection in silicon-based gradient metasurface structures using optimized anti-reflection coatings. Theoretical predictions of the optimum ARC material index and thickness were made, and the predictions were shown to be in good agreement with calculations based on the RCWA method. It has been demonstrated that anti-reflective coatings optimized for f=0.5 outperform the standard approach by a factor of 5 for metasurfaces below 73% areal fill fraction, and reflectance values below 0.5% are obtained for areal fill fractions below 88% using an ARC optimized for f=0.75. This work shows a path toward low-reflection metasurface optics, with an approach that is compatible with standard 2D fabrication methods involving a single patterning step.

CHAPTER 7: CONCLUSION

Transparent electrodes are important components in many optoelectronic devices such as photovoltaics and high-speed photodetectors. However, there is an intrinsic tradeoff between optical transparency and electrical conductivity for transparent electrodes, especially in metallic nanowire arrays. To address this issue, light trapping transparent electrodes are widely employed. In this dissertation, we have contributed several optical designs and characterized different aspects of their performance, demonstrating their potential for next generation transparent electrodes and other optoelectronic devices.

First, we numerically investigated the optical performance of triangular light trapping electrodes, including their size dependent, angle-dependent, and wavelength-dependent optical response. It was found that for silver electrodes on silicon embedded in a glass cover layer, with 2 μm width, 30° surface tilt and 10% areal metal coverage, a nearly polarization-independent spectrally averaged optical transmission of 90% is achieved across the visible spectrum. Owing to high conductivity of silver, the sheet resistance is as small as 0.22 Ω/sq, which satisfies typical industrial requirements.

A prototype transparent electrode structure was fabricated by multiphoton lithography and selective chemical deposition. Light trapping was demonstrated using optical microscopy, and significant shadowing reduction was demonstrated through spatial mapping of the light trapping efficiency. The results show that structures with surface tilt angles larger than half of the critical angle of the cover layer indeed achieve efficient light recovery, demonstrating the concept of light trapping via total internal reflection.

Though the triangular metallic nanowires exhibit broadband transmission enhancement by light trapping, the fabrication remains challenging. In Chapter 5 we proposed a novel type of light trapping electrode that uses a combination of grating-based light redirection and zero-order suppression. By judiciously engineering the geometry of the dielectric nanowires that form the grating, the zero order reflection is virtually eliminated through destructive interference, so that the incident light is only reflected at higher angles, enabling light trapping via total internal reflection. A spectrally averaged optical transmission of ~90% with near 55% shadowing reduction has been demonstrated. This proposed design was fabricated and prototype structures were characterized by optical microscopy, reflection spectroscopy, and linear laser scanning, revealing significant light trapping and near-zero reflection losses. The proposed design is compatible with standard fabrication methods, making the approach a promising candidate for real-world implementation.

Finally, transmissive light-redirecting devices were studied in this Dissertation. Metasurfaces enable the development of flat optical components that can replace traditional bulky optical elements. Subwavelength structures placed on a surface can impart arbitrary phase ptofiles to the wavefront, enabling the formation of ultrathin lenses, sensors, and beam steering elements. To improve the performance of metasurface-based optical elements, dedicated antireflective coatings must be developed that are compatible with common metasurface fabrication approaches. It was found through effective medium analysis that for metasurfaces with non-uniform index distributions, the traditional antireflective coating (ARC) design fails. An alternate approach was proposed that makes use of a lower index and larger thickness for the ARC. The optimized approach was shown to enable near-unity optical transmission across a wide range of metasurface

geometries. This work could help improve the performance of metasurface elements by minimizing reflection losses, and reducing the visibility of imaging artifacts that result from reflections inside optical systems.

Based on the presented work we expect the proposed light trapping approaches will help improve the performance of next-generation photonic devices through the inclusion of novel light trapping transparent electrodes, with applications including photovoltaics, optical sensors, and gradient metasurface based optical systems.

APPENDIX A: THIN-FILM TRANSMISSION AND CONDUCTIVITY

Drude model

To illustrate the intrinsic trade-off between conductivity and transparency discussed in Chapter 1, here we investigate the optical response of thin films. We will consider a generic conducting material described as a dielectric host doped with free charges. The free charge response is described by the Drude model [89, 90]. The relative permittivity of the film is given by:

$$\varepsilon_r(\omega) = \varepsilon_h - \frac{\omega_p^2}{\omega^2 + i\Gamma\omega} \tag{A-1}$$

where Γ is the damping rate of the metal and ω is the angular frequency of the incident light, ε_h is the permittivity of the host dielectric material and ω_p is the plasma frequency:

$$\omega_p = \sqrt{\frac{Ne^2}{\varepsilon_0 m}} \tag{A-2}$$

where N is the density of free electrons, e is the charge carried by a single electron, ε_0 is the vacuum permittivity and m is the electron mass. The real and imaginary part of the refractive index of this material follows from:

$$n(\omega) = \sqrt{\frac{1}{2}(|\varepsilon_r| + \varepsilon_r')} \qquad \text{(A-3)}$$

$$k(\omega) = \sqrt{\frac{1}{2}(|\varepsilon_r| - \varepsilon_r')} \qquad \text{(A-4)}$$

The properties of the thin films

The absorption coefficient of the material is given by:

$$\alpha(\omega) = 2\frac{\omega}{c}k(\omega) \qquad \text{(A-5)}$$

where c is the speed of light. When a thin film of this material is placed on a substrate, the reflectance and transmittance is given by:

$$R = |r_{012}|^2 = \left| \frac{r_{01} + r_{12}e^{-2ik_{z1}d}}{1 + r_{01}r_{12}e^{-2ik_{z1}d}} \right|^2 \qquad \text{(A-6)}$$

$$T = |t_{012}|^2 = \left| \frac{t_{01}t_{12}e^{-ik_{z1}d}}{1 + r_{01}r_{12}e^{-2ik_{z1}d}} \right|^2 \qquad \text{(A-7)}$$

where r_{ij} and t_{ij} is the Fresnel amplitude of reflection and transmission coefficient between the corresponding interfaces. k_{z1} is the propagating wave vector inside the film, and d is the film thickness, as shown in Figure A.1. The corresponding absorbance are hence obtained:

$$A = 1 - T - R \qquad \text{(A-8)}$$

94
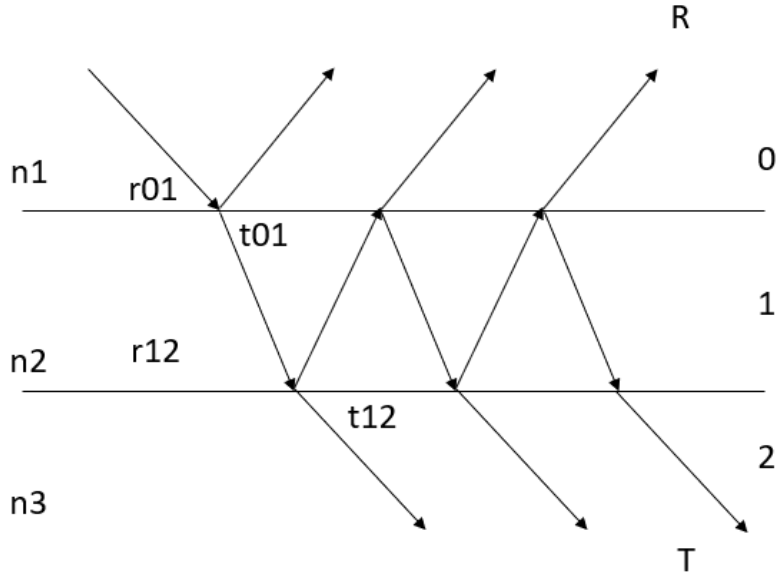
Figure A.1: Schematic of thin film reflection and transmission processes.

The scattering time of free electrons are defined by the damping rate that $\tau = \frac{1}{\Gamma}$. This affects both the optical response and the electrical conductivity. The low-frequency electrical conductivity is given by:

$$\sigma = \frac{Ne^2\tau}{m} \frac{1}{1-i\omega\tau} \tag{A-9}$$

for a continuous film of thickness d on an insulating substrate, the sheet conductivity of the film is given by:

$$\sigma_{sh} = \sigma d \tag{A-10}$$

Next, we evaluate the electrical performance and the normal-incidence optical transmission of red light (λ=632 nm) of a 1 μm thick film of this material deposited on a substrate with index

n=1.5. The results are shown in Figure A.2 as a function of free carrier density. When the carrier density increases, the optical transmittance is seen to decreases, while the sheet conductivity increases. For low carrier densities, the transmission loss is dominated by absorption losses. For high carrier densities, reflection loss dominates. This illustrates the need for different approaches for achieving transparent electrodes, depending on the type of conductor used.
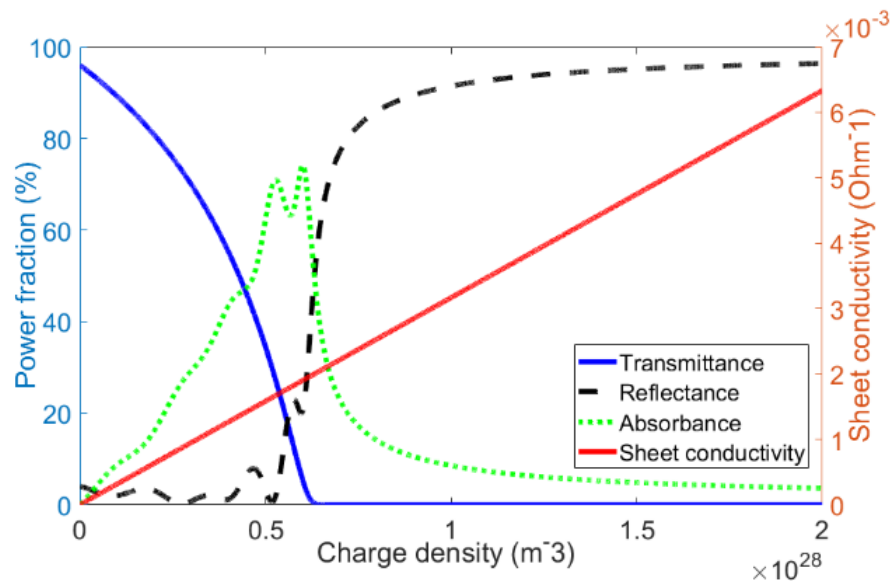
Figure A.2: Optical and electrical performance of a thin conducting film as a function of free carrier density.

In order to achieve high sheet conductivity, one could use a very thin film of highly conductive material, or a thick film of less conductive material. For typical conductive oxides, a continuous film with a thickness of hundreds of nanometers is typically used. However, to achieve acceptable transmission with a metallic film, a thickness of a few nm would be required, which is

challenging in practice. As shown in Figure A.3, a film thickness of 1 nm is required to achieve

88.6% transmittance when using a thin gold film as the conducting layer using λ=400 nm.
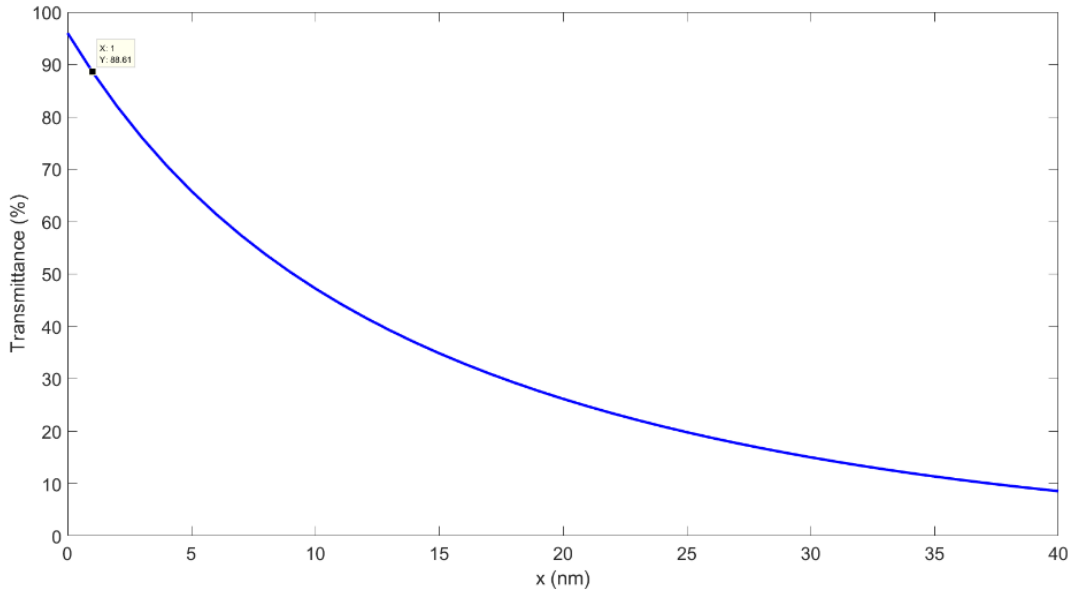
Figure A.3: Thickness dependent transmittance of thin gold film on a glass substrate

(n=1.5).

Because of the trade-off between conductivity and transmission, a typical ITO layer cannot

achieve high transmittance (T>90%) and low sheet resistance (R<10 Ω/sq.) at the same time [91].

Therefore, alternative approaches to thin film transparent electrodes that can achieve good optical

and electrical performance simultaneously are necessary. It is natural to consider condensing the

conductive materials in a small area while leaving large uncovered areas on the interface to

enhance optical transmission. Following this logic, random mesh electrodes and wire array

electrodes are presented. The schematics of both structures are shown in the right panel of Figure

A.4. To evaluate the optical performance of such wire electrodes, the transmission formula for thin

film electrodes given above is no longer appropriate. Instead, the optical transmission will be affected by the fraction of surface area covered by the electrodes, defined as the areal coverage f. Considering light incident on metallic contacts, most of the light is reflected, and a small fraction is dissipated. Assuming all the light incident on the contact surface will be either reflected or absorbed, the optical transmission into the underlying substrate will approximately simply be:

$$T = 1 - f \qquad (\text{A-11})$$

If the average thickness of the metallic wires is d, then the effective sheet resistance associated with a regular wire grid will be given by:

$$R_{sh} = \frac{\rho}{df} \qquad (\text{A-12})$$

where ρ is the resistivity of the material Combining Equation (A-11) and (A-12) we can easily obtain the relationship between transmittance and sheet resistance:

$$T = 1 - \frac{\rho}{R_{sh}d} \qquad (\text{A-13})$$

From Equation (A-13) we see that once the wire composition and thickness are set, there is still a balance between the optical transmittance and the sheet resistance. In general, this balance is affected by the size and shape of the individual wires and the areal coverage. The type of the material is another factor that significantly affects the optical and electrical performance. As shown in the left panel of Figure A.4, metallic nanowires (MNWs) can outperform thin-film electrodes made of transparent conductive oxides such as ITO.

APPENDIX B: RAY OPTICS MODEL OF TRIANGULAR ELECTRODES

The ray optics modal mentioned in Chapter 3 is developed by ray tracing. Detailed procedures are derived here.

Under oblique incidence, the internal incident angle inside the cover layer is given by Snell's Law:

$$\varphi = arc\sin\left(\frac{n_0}{n_2}\sin(\phi)\right) \tag{B-1}$$

When the light is incident from air in an oblique angle ϕ, it undergoes specular reflection on both left and right sides of the electrodes, resulting in rays travelling upward to the cover layer surface at different angles. If this angle is larger than the critical angle of the interface between the cover layer and air, TIR occurs and the light may be recovered. For angles below the critical angle the light trapping will be significantly reduced, which is expected to lead to significant shadowing losses. Therefore, the overall transmittance of the electrode array is derived:

$$T(\phi) = T_0(\phi)\left[1 - f + \frac{f}{2}\left(R_0(2\theta + \varphi)R(\theta + \varphi) + R_0(|2\theta - \varphi|)R(|\theta - \varphi|)\right)\right] \tag{B-2}$$

Interaction with the neighboring electrodes is another deleterious effect on the optical performance. When the electrodes are close enough, the recovered light can hit the neighboring electrodes and produce multiple reflections, resulting in additional optical losses. This effect can also be mitigated by ray optics model. To achieve interaction-free light recovery, light incident on both left and right side of the electrode should be redirected into the spacing between the electrodes. This requires that light reflected by an electrode neither hits the edge of this electrode

nor hits the neighboring electrodes. Hence the geometry of the electrode array should follow the following principle:

$$\begin{cases} D\tan(2\theta + \varphi) + (D + h)\tan(2\theta + \varphi) \geq W \\ (D + h)\tan(2\theta + \varphi) \leq \dfrac{W}{f} - W \end{cases}$$ (B-3)
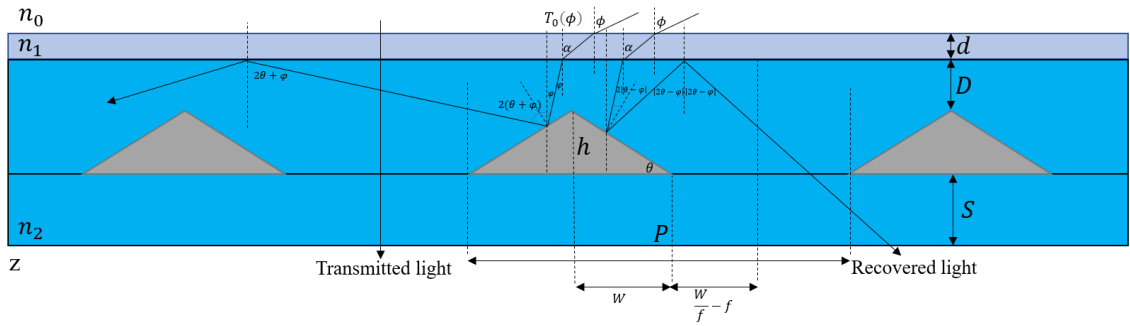
Figure B.1: Sketch of the geometry of the light-trapping electrodes.

As shown in Figure B.1, these inequalities formulate the geometrical requirements on the left side of the electrodes. Assume that:

$$D_1(\varphi) = w/2 \left[cot(2\theta + \varphi) - \tan(\theta)\right]$$ (B-4)

$$D_2(\varphi) = w \left[\left(\frac{1}{f} - 1\right) cot(2\theta + \varphi) - \tan(\theta)\right]$$ (B-5)

As $D_1(\varphi)$ corresponds to the situation of hitting the electrode edge, $D_2(\varphi)$ is related to hitting the neighboring electrodes. Equation (B-4) and (B-5) mark the range of D that allows for interaction-free light recovery. Then Equation (B-3) is then converted to

101

$$D_1(\varphi) < D < D_2(\varphi) D_2(\varphi) \geq 0 \tag{B-6}$$

Similarly, the reflection angle becomes |2θ-φ| instead of 2θ+φ on the right side of the electrodes, thus we have:

$$D_1(-\varphi) < D < D_2(-\varphi) \cap D_2(-\varphi) \geq 0 \tag{B-7}$$

Next, we need to compare the value of D_1 and D_2 under different incident angles to determine the available range of D. When the reflected light reaches the top boundary, |2θ-φ| and 2θ+φ are both within the angular range from 0 to 90°, then (B-4) and (B-5) are monotonically decreasing:

$$D_1(-\varphi) > D_1(0) > D_1(\varphi) \tag{B-8}$$

$$D_2(-\varphi) > D_2(0) < D_2(\varphi) \tag{B-9}$$

Equation (B-8) and (B-9) indicate that the incident light is more squeezed on the right side than on the left side such that larger D is required to avoid contact with the electrode edge. It also means that the incident light can travel longer distance before hitting the neighboring electrodes on the right side. The maximum internal angle φ_{max}, also known as the critical angle, is obtained at 90° incidence, then the range of D is determined from (B-6)-(B-9):

$$D_1(-\varphi_{max}) < D < D_2(\varphi_{max}) \tag{B-10}$$

Due to the monotonicity of function (B-4) and (B-5), the range from any incident angle smaller than φ_{max} is contained in (B-10). Then the geometrical requirement of achieving interaction-free light recovery is obtained:

$$D_1(-\varphi_{max}) < D_2(\varphi_{max}) \cap D_2(\varphi_{max}) > 0 \tag{B-11}$$

It is found that f, θ and n_2 are contained in (B-4) and (B-5). Therefore, with (B-11) we can further optimize the design of the light trapping electrodes. Accordingly, the detailed expression of η is shown as:

$$\eta = \frac{R_0(2\theta+\varphi)R(\theta+\varphi)+R_0(|2\theta-\varphi|)R(|\theta-\varphi|)}{2} \tag{B-12}$$

From Equation (B-12), it is found that this definition excludes the influence of the top interface, which results in little transmission at large incident angles.

APPENDIX C: SEM IMAGES AND COMPOSITION ANALYSIS OF TRIANGULAR LIGHT-TRAPPING ELECTRODES

As discussed in Chapter 4, energy dispersive X-ray spectroscopy (EDS) was used to confirm selective deposition of copper on the electrodes. K_α lines of Cu and Si were used to generate elemental maps shown in Figure C.1(b) and (c), respectively. Figure C.1(b) shows that copper is selectively deposited on the electrodes. Figure C.1(c) shows intensity of Si (from the borosilicate glass substrate).
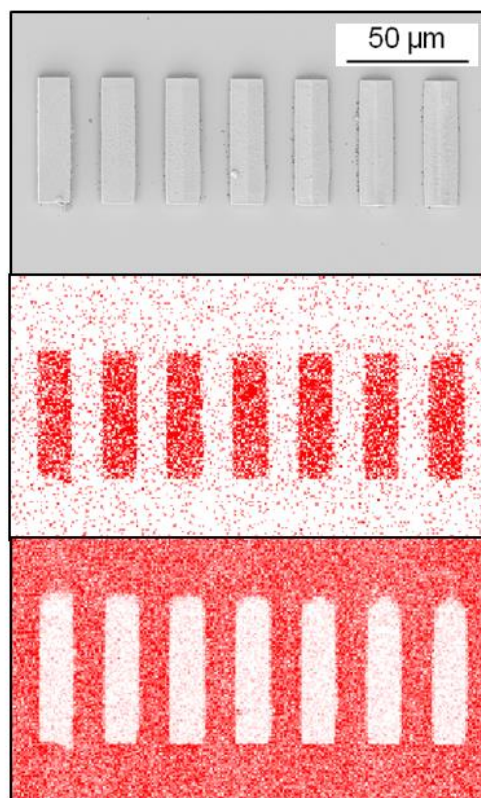
Figure C.1: (a) SEM, (b) Cu K_α EDS, and (c) Si K_α EDS map of the angle array. Cu and Si are both shown in red versus white background.

APPENDIX D: RIGOROUS MODAL ANALYSIS OF DIELECTRIC GRATINGS

The grating mode profiles in Chapter 5 are obtained by rigorous modal analysis. The detailed procedures are discussed here.

First, we consider a 1-D dielectric grating with periodic index distribution along the x-axis, as shown in Figure D.1.
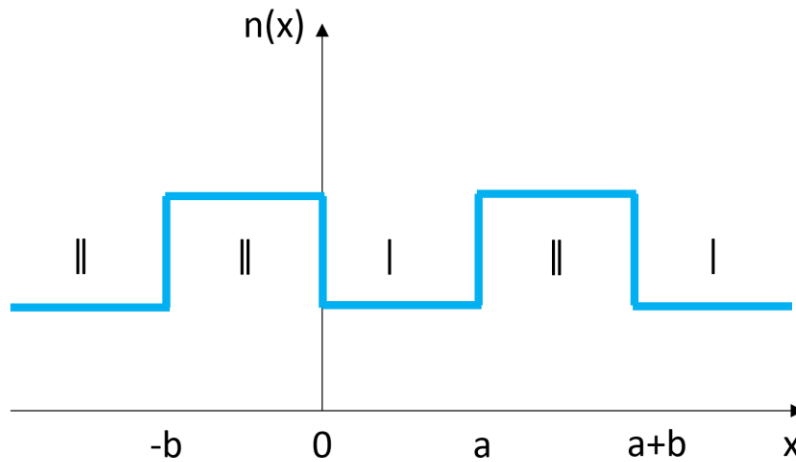
Figure D.1: The refractive index distribution of a 1-D dielectric grating.

In the grating, each unit cell is comprised of two regions. For example, in a unit cell extending from x=-b to x=a, region I (x=0 to x=a) is the spacing between the dielectric blocks that has lower refractive index n_1, while region II (x=-b to x=0) is the block with higher index n_2. The field distribution inside the grating is expressed in 1-D Helmholtz equation:

$$\frac{d^2}{dx^2}E(x) + k_x^2 E(x) = 0 \qquad (D-1)$$

The wavevector k has two components k_x and k_z. k_z remains invariant since there is no index variation along z-axis. Then Equation (D-1) can be rewritten as:

$$\begin{cases} \frac{d^2}{dx^2}E(x) + (k_0^2 n_1^2 - k_z^2)E(x) = 0, \ 0 < x < a \\ \frac{d^2}{dx^2}E(x) + (k_0^2 n_2^2 - k_z^2)E(x) = 0, \ -b < x < 0 \end{cases} \qquad \text{(D-2)}$$

At normal incidence, there is no additional k_x component from the incident light, so the solution to Equation (D-2) is given by:

$$\begin{cases} u_1(x) = Ae^{j\alpha x} + Be^{-j\alpha x}, \ 0 < x < a \\ u_2(x) = Ce^{j\beta x} + De^{-j\beta x}, \ -b < x < 0 \end{cases} \qquad \text{(D-3)}$$

$u_1(x)$ and $u_2(x)$ are the field distributions in region I and II respectively. Where $\alpha = \sqrt{k_0^2 n_1^2 - k_z^2}$ and $\beta = \sqrt{k_0^2 n_2^2 - k_z^2}$. It is evident that the E-field is consist of both forward-propagating and counter-propagating modes with identical propagation constant in each region, so the net value of k_x is zero.

Considering the continuity of the field amplitude and the slope. We have the following relations: $u_1(0) = u_2(0), u_1'(0) = u_2'(0), u_1(a) = u_2(-b), u_1'(a) = u_2'(-b)$. Substitute these relations into Equation (D-3) we have:

$$\begin{cases} A + B - C - D = 0 \\ \alpha A - \alpha B - \beta C + \beta D = 0 \\ Ae^{j\alpha a} + Be^{-j\alpha a} - Ce^{-j\beta b} - De^{j\beta b} = 0 \\ \alpha Ae^{j\alpha a} - \alpha Be^{-j\alpha a} - \beta Ce^{-j\beta b} + \beta De^{j\beta b} = 0 \end{cases} \qquad \text{(D-4)}$$

The solutions of Equation (D-4) are given if the determinant of the equation is zero:

$$\begin{vmatrix} 1 & 1 & -1 & -1 \\ \alpha & -\alpha & -\beta & \beta \\ e^{j\alpha a} & e^{-j\alpha a} & -e^{-j\beta b} & -e^{j\beta b} \\ \alpha e^{j\alpha a} & -\alpha e^{-j\alpha a} & -\beta e^{-j\beta b} & \beta e^{j\beta b} \end{vmatrix} = 0 \qquad (D\text{-}5)$$

Working through the determinant and grouping the exponentials, Equation (D-5) is rewritten as:

$$\frac{-(\alpha^2+\beta^2)}{2\alpha\beta} \sin(\alpha a) \sin(\beta b) + \cos(\alpha a) \cos(\beta b) - 1 = 0 \qquad (D\text{-}6)$$

All grating modes are solutions to Equation (D-6). Since k_z is contained in α and β, for each mode k_z can be numerically solved. Then the corresponding propagation phase shift inside the gratings can be calculated.

The field distribution along the gratings can also be derived. Recall Equation (D-3), the normalized field distribution is expressed in terms of the ratio between coefficients A, B, C and D:

$$\begin{cases} u_1(x) = \frac{A}{B} e^{j\alpha x} + e^{-j\alpha x}, \ 0 < x < a \\ u_2(x) = \frac{C}{D} e^{j\beta x} + e^{-j\beta x}, \ -b < x < 0 \end{cases} \qquad (D\text{-}7)$$

where $\frac{A}{B}$ and $\frac{C}{D}$ are obtained from Equation (D-4):

$$\begin{cases} \dfrac{A}{B} = \dfrac{-2\beta e^{-j\alpha a}-(\alpha-\beta)e^{-j\beta b}+(\alpha+\beta)e^{j\beta b}}{2\beta e^{-j\alpha a}-(\alpha+\beta)e^{-j\beta b}+(\alpha-\beta)e^{j\beta b}} \\[2ex] \dfrac{C}{D} = \dfrac{2\alpha e^{j\beta b}-(\alpha-\beta)e^{j\alpha a}-(\alpha+\beta)e^{-j\alpha a}}{-2\alpha e^{-j\beta b}+(\alpha+\beta)e^{j\alpha a}+(\alpha-\beta)e^{j\beta b}} \end{cases} \qquad \text{(D-8)}$$

Similarly, k_z and the field distribution can also be obtained at TM polarization by replacing α with $\alpha/n_1{}^2$ and β with $\beta/n_1{}^2$ in Equation (D-6) and (D-8), except for the exponential and sinusoidal terms.

APPENDIX E: LIST OF PUBLICATIONS

1) M. Sun and P. G. Kik, "*Scale dependent performance of metallic light-trapping transparent electrodes*" Optics Express 28, 18112-18121 (2020)

2) M. Sun and P. G. Kik, "*Light trapping transparent electrodes with a wide-angle response*" Optics Express 29, 24989-24999 (2021)

3) M. J. Hossain, M. Sun, G. Doerk, P. G. Kik and K. O. Davis, "*Self-Assembled Multifunctional Nanostructures for Surface Passivation and Photon Management in Silicon Photovoltaics*" *Nanophotonics*, vol. 10, no. 18, 2021, pp. 4611-4621. https://doi.org/10.1515/nanoph-2021-0472

4) M. Sun, P. Golvari, S. M. Kuebler, and P. G. Kik, "*Experimental demonstration of light trapping transparent electrodes*", to be submitted.

5) M. Sun, D. Huang, P. Golvari, S. M. Kuebler, P. J. Delfyett, and P. G. Kik, "*Efficient grating-based light trapping electrodes using selective zero order suppression*", to be submitted.

6) M. Sun and P. G. Kik, "*Suppression of reflection loss in gradient metasurface optical elements*", to be submitted.

7) M. J. Hossain, M. Sun, P. G. Kik and K. O. Davis, "*Photon Management in Silicon Photovoltaic Cells*", to be submitted.

APPENDIX F: COPYRIGHT PERMISSION LETTERS

AUTHOR AND END-USER REUSE POLICY

Our policies afford authors, their employers, and third parties the right to reuse the author's Accepted Manuscript (AM) or the final publisher Version of Record (VoR) of the article as outlined below:

Reuse purpose	Article version that can be used under:		
	Copyright Transfer	Open Access Publishing Agreement	CC BY License
Reproduction by authors in a compilation or for teaching purposes short term	AM	VoR	VoR
Posting by authors on arXiv or other preprint servers after publication (posting of preprints before or during consideration is also allowed)	AM	VoR	VoR
Posting by authors on a non-commercial personal website or closed institutional repository (access to the repository is limited solely to the institutions' employees and direct affiliates (e.g., students, faculty), and the repository does not depend on payment for access, such as subscription or membership fees)	AM	VoR	VoR
Posting by authors on an open institutional repository or funder repository	AM after 12 month embargo	VoR	VoR
Reproduction by authors or third party users for non-commercial personal or academic purposes (includes the uses listed above and e.g. creation of derivative works, translation, text and data mining)	Authors as above, otherwise by permission only. Contact copyright@optica.org.	VoR	VoR
Any other purpose, including commercial reuse on such sites as ResearchGate, Academia.edu, etc. and/or for sales and marketing purposes	By permission only. Contact copyright@optica.org.	By permission only. Contact copyright@optica.org	VoR

In addition, we allow authors to post their manuscripts on the Cornell University Library's arXiv site prior to submission to Optica Publishing Group's journals.

114

REFERENCES

1. Liu, Z., et al., *Flexible electronics based on inorganic nanowires.* Chem Soc Rev, 2015. **44**(1): p. 161-92.

2. Kou, P., et al., *Improved Flexible Transparent Conductive Electrodes based on Silver Nanowire Networks by a Simple Sunlight Illumination Approach.* Sci Rep, 2017. **7**: p. 42052.

3. Sannicolo, T., et al., *Metallic Nanowire-Based Transparent Electrodes for Next Generation Flexible Devices: a Review.* Small, 2016. **12**(44): p. 6052-6075.

4. Ellmer, K., *Past achievements and future challenges in the development of optically transparent electrodes.* Nature Photonics, 2012. **6**(12): p. 809-817.

5. Blakers, A.W., *Shading losses of solar‐cell metal grids.* Journal of Applied Physics, 1992. **71**(10): p. 5237-5241.

6. Zhang, H.L., et al., *Photovoltaics: reviewing the European Feed-in-Tariffs and changing PV efficiencies and costs.* ScientificWorldJournal, 2014. **2014**: p. 404913.

7. Yoon, Y.H., et al., *Transparent Film Heater Using Single-Walled Carbon Nanotubes.* Advanced Materials, 2007. **19**(23): p. 4284-4287.

8. Sui, D., et al., *Flexible and transparent electrothermal film heaters based on graphene materials.* Small, 2011. **7**(22): p. 3186-92.

9. Li, J., et al., *A Flexible and Transparent Thin Film Heater Based on a Silver Nanowire/Heat-resistant Polymer Composite.* Macromolecular Materials and Engineering, 2014. **299**(11): p. 1403-1409.

10. Fujikawa, Y., et al., *Camera built-in type rearview mirror device*. 2005, Google Patents.

11. Hosono, H. and K. Ueda, *Transparent Conductive Oxides*, in *Springer Handbook of Electronic and Photonic Materials*. 2017. p. 1-1.

12. Dai, Q., et al., *Transparent liquid-crystal-based microlens array using vertically aligned carbon nanofiber electrodes on quartz substrates.* Nanotechnology, 2011. **22**(11): p. 115201.

13. Xue, J., et al., *Nanowire-based transparent conductors for flexible electronics and optoelectronics.* Science Bulletin, 2017. **62**(2): p. 143-156.

14. Askari, H., et al., *Electrical and optical properties of ITO thin films prepared by DC magnetron sputtering for low-emitting coatings.* 2014.

15. Hecht, D.S., L. Hu, and G. Irvin, *Emerging transparent electrodes based on thin films of carbon nanotubes, graphene, and metallic nanostructures.* Adv Mater, 2011. **23**(13): p. 1482-513.

16. Sharma, A., G. Andersson, and D.A. Lewis, *Role of humidity on indium and tin migration in organic photovoltaic devices.* Phys Chem Chem Phys, 2011. **13**(10): p. 4381-7.

17. Zhang, R. and M. Engholm, *Recent Progress on the Fabrication and Properties of Silver Nanowire-Based Transparent Electrodes.* Nanomaterials (Basel), 2018. **8**(8).

18. Hanson, E.L., et al., *Advanced Surface Modification of Indium Tin Oxide for Improved Charge Injection in Organic Devices.* Journal of the American Chemical Society, 2005. **127**(28): p. 10058-10062.

19. Roberts, M.W., et al., *Continuum Plate Theory and Atomistic Modeling to Find the Flexural Rigidity of a Graphene Sheet Interacting with a Substrate.* 2010. **2010**: p. 1-8.

20.   Castro Neto, A.H., et al., *The electronic properties of graphene.* Reviews of Modern Physics, 2009. **81**(1): p. 109-162.

21.   *Index for Volume 5*, in *Handbook of Nanostructured Materials and Nanotechnology*, H.S. Nalwa, Editor. 2000, Academic Press: Burlington. p. 769-778.

22.   Ziadan, K., *Conducting Polymers Application.* 2012. p. 1-26.

23.   Vosgueritchian, M., D.J. Lipomi, and Z. Bao, *Highly Conductive and Transparent PEDOT:PSS Films with a Fluorosurfactant for Stretchable and Flexible Transparent Electrodes.* Advanced Functional Materials, 2012. **22**(2): p. 421-428.

24.   Le, T.-H., Y. Kim, and H. Yoon, *Electrical and Electrochemical Properties of Conducting Polymers.* Polymers, 2017. **9**(4): p. 150.

25.   Eatemadi, A., et al., *Carbon nanotubes: properties, synthesis, purification, and medical applications.* Nanoscale research letters, 2014. **9**(1): p. 393-393.

26.   Arici, E. and S. Karazhanov, *Carbon nanotubes for organic/inorganic hybrid solar cells.* Materials Science in Semiconductor Processing, 2016. **41**: p. 137-149.

27.   Zhou, Y. and R. Azumi, *Carbon nanotube based transparent conductive films: progress, challenges, and perspectives.* Science and technology of advanced materials, 2016. **17**(1): p. 493-516.

28.   Jensen, B.D., et al., *Simulating the effects of carbon nanotube continuity and interfacial bonding on composite strength and stiffness.* Composites science and technology, 2018. **166**: p. 10-19.

29.   Jiang, S., et al., *Ultrahigh-performance transparent conductive films of carbon-welded isolated single-wall carbon nanotubes.* Science Advances, 2018. **4**(5): p. eaap9264.

30.   Hosseini, S.V., H. Arabi, and A. Kompany, *Comparison of hydrogen absorption in metallic and semiconductor single-walled Ge- and GeO2-doped carbon nanotubes.* International Journal of Hydrogen Energy, 2017. **42**(2): p. 969-977.

31.   Lah, N.A.C. and S. Trigueros, *Synthesis and modelling of the mechanical properties of Ag, Au and Cu nanowires.* Sci Technol Adv Mater, 2019. **20**(1): p. 225-261.

32.   Ye, S., et al., *Metal nanowire networks: the next generation of transparent conductors.* Adv Mater, 2014. **26**(39): p. 6670-87.

33.   Tokuno, T., et al., *Hybrid transparent electrodes of silver nanowires and carbon nanotubes: a low-temperature solution process.* Nanoscale research letters, 2012. **7**(1): p. 281-281.

34.   Garnett, E.C., et al., *Self-limited plasmonic welding of silver nanowire junctions.* Nat Mater, 2012. **11**(3): p. 241-9.

35.   Hu, L., et al., *Scalable Coating and Properties of Transparent, Flexible, Silver Nanowire Electrodes.* ACS Nano, 2010. **4**(5): p. 2955-2963.

36.   Langley, D.P., et al., *Metallic nanowire networks: effects of thermal annealing on electrical resistance.* Nanoscale, 2014. **6**(22): p. 13535-43.

37.   De, S., et al., *Size effects and the problem with percolation in nanostructured transparent conductors.* ACS Nano, 2010. **4**(12): p. 7064-72.

38.   Saive, R. and H.A. Atwater, *Mesoscale trumps nanoscale: metallic mesoscale contact morphology for improved light trapping, optical absorption and grid conductance in silicon solar cells.* Opt Express, 2018. **26**(6): p. A275-A282.

39.   Pendry, J.B., D. Schurig, and D.R. Smith, *Controlling Electromagnetic Fields.* Science, 2006. **312**(5781): p. 1780.

40.   Schumann, M.F., et al., *Cloaked contact grids on solar cells by coordinate transformations: designs and prototypes.* Optica, 2015. **2**(10).

41.   Kik, P.G., *Catoptric electrodes: transparent metal electrodes using shaped surfaces.* Opt Lett, 2014. **39**(17): p. 5114-7.

42.   Zhao, Z., K.X. Wang, and S. Fan, *Analysis of an anti-reflecting nanowire transparent electrode for solar cells.* Journal of Applied Physics, 2017. **121**(11).

43.   Khorasaninejad, M., et al., *Metalenses at visible wavelengths: Diffraction-limited focusing and subwavelength resolution imaging.* Science, 2016. **352**(6290): p. 1190-1194.

44.   Pahlevaninezhad, H., et al., *Nano-optic endoscope for high-resolution optical coherence tomography in vivo.* Nature Photonics, 2018. **12**(9): p. 540-547.

45.   Guo, Q., et al., *Compact single-shot metalens depth sensors inspired by eyes of jumping spiders.* Proceedings of the National Academy of Sciences, 2019. **116**(46): p. 22959-22965.

46.   Holsteen, A.L., et al., *A Light-Field Metasurface for High-Resolution Single-Particle Tracking.* Nano Letters, 2019. **19**(4): p. 2267-2271.

47.   Wei, Z., et al., *Highly efficient beam steering with a transparent metasurface.* Optics Express, 2013. **21**(9): p. 10739-10745.

48.   Kamali, S.M., et al., *Angle-Multiplexed Metasurfaces: Encoding Independent Wavefronts in a Single Metasurface under Different Illumination Angles.* Physical Review X, 2017. **7**(4): p. 041056.

49.   Lee, G.-Y., et al., *Metasurface eyepiece for augmented reality.* Nature Communications, 2018. **9**(1): p. 4562.

50.   Huang, Y.-W., et al., *Gate-Tunable Conducting Oxide Metasurfaces.* Nano Letters, 2016. **16**(9): p. 5319-5325.

51.   Wang, Y., et al., *Electrical tuning of phase-change antennas and metasurfaces.* Nature Nanotechnology, 2021. **16**(6): p. 667-672.

52.   Zhang, Y., et al., *Electrically reconfigurable non-volatile metasurface using low-loss optical phase-change material.* Nature Nanotechnology, 2021. **16**(6): p. 661-666.

53.   Sun, M. and P.G. Kik, *Scale dependent performance of metallic light-trapping transparent electrodes.* Optics Express, 2020. **28**(12): p. 18112-18121.

54.   Martin, O.J.F., *Plasmon Resonances in Nanowires with a Non—regular Cross-Section*, in *Optical Nanotechnologies: The Manipulation of Surface and Local Plasmons*, J. Tominaga and D.P. Tsai, Editors. 2003, Springer Berlin Heidelberg. p. 183-210.

55.   Gordon, R.G., *Criteria for Choosing Transparent Conductors.* MRS Bulletin, 2011. **25**(08): p. 52-57.

56.   Haacke, G., *New figure of merit for transparent conductors.* Journal of Applied Physics, 1976. **47**(9): p. 4086-4089.

57.   Shim, B.S., et al., *Transparent conductors from layer-by-layer assembled SWNT films: importance of mechanical properties and a new figure of merit.* ACS Nano, 2010. **4**(7): p. 3725-34.

58.   Ghosh, D.S., T.L. Chen, and V. Pruneri, *High figure-of-merit ultrathin metal transparent electrodes incorporating a conductive grid.* Applied Physics Letters, 2010. **96**(4): p. 041109.

59.   Sun, M. and P.G. Kik, *Light trapping transparent electrodes with a wide-angle response.* Optics Express, 2021. **29**(16): p. 24989-24999.

60.   CST Studio Suite, Dassault Systèmes Simulia, Providence, Rhode Island, 2017.

61.   Moharam, M.G. and T.K. Gaylord, *Rigorous coupled-wave analysis of planar-grating diffraction.* Journal of the Optical Society of America, 1981. **71**(7): p. 811-818.

62.   Li, D., et al., *A Simple Strategy towards Highly Conductive Silver-Nanowire Inks for Screen-Printed Flexible Transparent Conductive Films and Wearable Energy-Storage Devices.* Advanced Materials Technologies, 2019. **4**(8): p. 1900196.

63.   Xu, X., et al., *Screen printed silver nanowire and graphene oxide hybrid transparent electrodes for long-term electrocardiography monitoring.* Journal of Physics D: Applied Physics, 2019. **52**(45): p. 455401.

64.   Malitson, I.H., *Interspecimen Comparison of the Refractive Index of Fused Silica*,†.* Journal of the Optical Society of America, 1965. **55**(10): p. 1205-1209.

65.   Malitson, I.H., *Interspecimen Comparison of the Refractive Index of Fused Silica.* Journal of the Optical Society of America, 1965. **55**(10): p. 1205-1209.

66.   Aspnes, D.E. and A.A. Studna, *Dielectric functions and optical parameters of Si, Ge, GaP, GaAs, GaSb, InP, InAs, and InSb from 1.5 to 6.0 eV.* Physical Review B, 1983. **27**(2): p. 985-1009.

67. Dodge, M.J., *Refractive properties of magnesium fluoride.* Applied Optics, 1984. **23**(12): p. 1980-1985.

68. Pastrňák, J. and L. Roskovcová, *Refraction Index Measurements on AlN Single Crystals.* physica status solidi (b), 1966. **14**(1): p. K5-K8.

69. ASTM Standard G173, Standard Tables for Reference Solar Spectral Irradiances: Direct Normal and Hemispherical on 37° Tilted Surface, American Society for Testing and Materials, West Conshocken, PA, USA.

70. Chu, H.-C., et al., *Spray-Deposited Large-Area Copper Nanowire Transparent Conductive Electrodes and Their Uses for Touch Screen Applications.* ACS Applied Materials & Interfaces, 2016. **8**(20): p. 13009-13017.

71. Zhang, R. and M. Engholm, *Recent Progress on the Fabrication and Properties of Silver Nanowire-Based Transparent Electrodes.* Nanomaterials, 2018. **8**(8): p. 628.

72. Park, S.-h., D.Y. Yang, and K.-s. Lee, *Tw• photon stereolithography for realizing ultraprecise thre… dimensional nano/microdevices.* Laser & Photonics Reviews, 2009. **3**: p. 1-11.

73. Farrer, R.A., et al., *Selective functionalization of 3-D polymer microstructures.* Journal of the American Chemical Society, 2006. **128**(6): p. 1796-1797.

74. Tal, A., et al., *Fabrication and characterization of three-dimensional copper metallodielectric photonic crystals.* Optics Express, 2007. **15**(26): p. 18283-18293.

75. Golvari, P. and S.M. Kuebler, *Fabrication of Functional Microdevices in SU-8 by Multi-Photon Lithography.* Micromachines, 2021. **12**(5): p. 472.

76. Clukay, C.J., et al., *Controlling formation of gold nanoparticles generated in situ at a polymeric surface.* Applied Surface Science, 2014. **292**: p. 128-136.

77. Barranco, A., et al., *Perspectives on oblique angle deposition of thin films: From fundamentals to devices.* Progress in Materials Science, 2016. **76**: p. 59-153.

78. Ordouie, E., H. Alisafaee, and A. Siahmakoun, *Ultracompact polarizing beam splitter based on single-material birefringent photonic crystal.* Optics letters, 2018. **43**(17): p. 4288-4291.

79. Johnson, P.B. and R.W. Christy, *Optical Constants of the Noble Metals.* Physical Review B, 1972. **6**(12): p. 4370-4379.

80. Botten, I.C., et al., *The Dielectric Lamellar Diffraction Grating.* Optica Acta: International Journal of Optics, 1981. **28**(3): p. 413-428.

81. Pierce, D.T. and W.E. Spicer, *Electronic Structure of Amorphous Si from Photoemission and Optical Studies.* Physical Review B, 1972. **5**(8): p. 3017-3029.

82. Wu, P.C., et al., *Near-Infrared Active Metasurface for Dynamic Polarization Conversion.* Advanced Optical Materials, 2021. **9**(16): p. 2100230.

83. Kamali, S.M., et al., *Highly tunable elastic dielectric metasurface lenses.* Laser & Photonics Reviews, 2016. **10**(6): p. 1002-1008.

84. Schlickriede, C., et al., *Imaging through Nonlinear Metalens Using Second Harmonic Generation.* Advanced Materials, 2018. **30**(8): p. 1703843.

85. Schonbrun, E., K. Seo, and K.B. Crozier, *Reconfigurable Imaging Systems Using Elliptical Nanowires.* Nano Letters, 2011. **11**(10): p. 4299-4303.

86. Zuo, H., et al., *High-Efficiency All-Dielectric Metalenses for Mid-Infrared Imaging.* Advanced Optical Materials, 2017. **5**(23): p. 1700585.

87. Kamali, S.M., Arbabi, E., Arbabi, A., Horie, Y. and Faraon, A. (2016), Highly tunable elastic dielectric metasurface lenses. Laser & Photonics Reviews, 10: 1002-1008. Copyright Wiley-VCH GmbH. Reproduced with permission.

88. Kikuta, H., et al., *Effective medium theory of two-dimensional subwavelength gratings in the non-quasi-static limit.* Journal of the Optical Society of America A, 1998. **15**(6): p. 1577-1585.

89. Drude, P., *Zur Elektronentheorie der Metalle.* Annalen der Physik, 1900. **306**(3): p. 566-613.

90. Drude, P., *Zur Elektronentheorie der Metalle; II. Teil. Galvanomagnetische und thermomagnetische Effecte.* Annalen der Physik, 1900. **308**(11): p. 369-402.

91. Lee, J.-Y., et al., *Solution-Processed Metal Nanowire Mesh Transparent Electrodes.* Nano Letters, 2008. **8**(2): p. 689-692.